

# Early Stopping for Deep Image Prior

Hengkang Wang<sup>1</sup>, Taihui Li<sup>1</sup>, Zhong Zhuang<sup>2</sup>, Tiancong Chen<sup>1</sup>, Hengyue Liang<sup>2</sup>  
and Ju Sun<sup>1</sup>

<sup>1</sup>Computer Science and Engineering, University of Minnesota, Minneapolis, USA.

<sup>2</sup>Electrical and Computer Engineering, University of Minnesota, Minneapolis, USA.

Contributing authors: [wang9881@umn.edu](mailto:wang9881@umn.edu); [lix5027@umn.edu](mailto:lix5027@umn.edu); [zhuan143@umn.edu](mailto:zhuan143@umn.edu);  
[chen6271@umn.edu](mailto:chen6271@umn.edu); [liang656@umn.edu](mailto:liang656@umn.edu); [jusun@umn.edu](mailto:jusun@umn.edu);

## Abstract

Deep image prior (DIP) and its variants have showed remarkable potential for solving inverse problems in computer vision, *without any extra training data*. Practical DIP models are often substantially overparameterized. During the fitting process, these models learn mostly the desired visual content first, and then pick up the potential modeling and observational noise, i.e., overfitting. Thus, the practicality of DIP hinges on good early stopping (ES) that captures the transition period. In this regard, the majority of DIP works for vision tasks only demonstrates the potential of the models—reporting the peak performance against the ground truth, but provides no clue about how to operationally obtain near-peak performance without access to the groundtruth. In this paper, we set to break this practicality barrier of DIP, and propose an efficient ES strategy which consistently detects near-peak performance across several vision tasks and DIP variants. Based on a simple measure of dispersion of consecutive DIP reconstructions, our ES method not only outpaces the existing ones—which only work in very narrow domains, but also remains effective when combined with a number of methods that try to mitigate the overfitting. The code to reproduce our experimental results is available at [https://github.com/sun-umn/Early\\_Stopping\\_for\\_DIP](https://github.com/sun-umn/Early_Stopping_for_DIP).

**Keywords:** early stopping, deep image prior, deep generative models, overparametrization, overfitting

## 1 Introduction

Inverse problems (IPs) are prevalent in computer vision, from basic image denoising, super-resolution, deblurring, to advanced 3D reconstruction and major tasks in computational photography and imaging (Szeliski, 2021). Despite the disparate settings, all these problems take the form of recovering a visual object  $\mathbf{x}$  from  $\mathbf{y} = f(\mathbf{x})$ , where  $f$  models the forward process to obtain the observation  $\mathbf{y}$ . Typically, these visual IPs are underdetermined:  $\mathbf{x}$  cannot be uniquely

determined from  $\mathbf{y}$ . This is exacerbated by potential modeling (e.g., linear  $f$  to approximate a nonlinear process) and observational (e.g., Gaussian or shot) noise, i.e.,  $\mathbf{y} \approx f(\mathbf{x})$ . To overcome the nonuniqueness and improve noise stability, people often encode a variety of problem-specific priors on  $\mathbf{x}$  when formulating IPs.

Traditionally, IPs are phrased as regularized data-fitting problems:

$$\min_{\mathbf{x}} \underbrace{\ell(\mathbf{y}, f(\mathbf{x}))}_{\text{data-fitting}} + \lambda \underbrace{R(\mathbf{x})}_{\text{regularizer (reg.)}}, \quad (1)$$

**Table 1** List of Common Acronyms (in alphabetic order)

CNN	convolutional neural network
DD	deep decoder
DIP	deep image prior
DIP-TV	DIP with total variation regularization
DL	deep learning
DNN	deep neural network
ELTO	early-learning-then-overfitting
ES	early stopping
EMV	exponential moving variance
GP-DIP	Gaussian process DIP
IP	inverse problem
MSE	mean squared error
PSNR	peak signal-to-noise ratio
SIREN	sinusoidal representation networks
SOTA	state-of-the-art
VAR	variance
WMV	windowed moving variance

where  $\lambda$  is the regularization parameter. Here, the loss  $\ell$  is chosen according to the noise model, and the regularizer  $R$  encodes priors on  $\mathbf{x}$ . The advent of deep learning (DL) has revolutionized how IPs are solved: on the radical side, deep neural networks (DNNs) are trained to directly map any given  $\mathbf{y}$  to an  $\mathbf{x}$ ; on the mild side, pretrained DL models are taken to replace certain nonlinear mappings in optimization algorithms to solve (1) (e.g., plug-and-play, and algorithm unrolling). We refer the reader to the recent surveys Janai, Güney, Behl, and Geiger (2020); Ongie et al. (2020) on these developments—they all trust large training sets  $\{(\mathbf{y}_i, \mathbf{x}_i)\}$  to sufficiently represent the underlying priors and/or noise distributions. *This paper concerns another family of striking ideas that parametrize  $\mathbf{x}$  using DNNs and require no extra training data.*

## 1.1 Deep image prior (DIP)

The idea (Ulyanov, Vedaldi, & Lempitsky, 2018) is simple: parameterize  $\mathbf{x}$  as  $\mathbf{x} = G_{\theta}(\mathbf{z})$ , where  $G_{\theta}$  is a trainable DNN parametrized by  $\theta$  and  $\mathbf{z}$  is a trainable or frozen random seed, put it into (1) and optionally remove the regularizer:

$$\min_{\theta} \ell(\mathbf{y}, f(G_{\theta}(\mathbf{z}))). \quad (2)$$

$G_{\theta}$  is often significantly “overparameterized”—containing substantially more parameters than the dimension of  $\mathbf{x}$ , and the resulting optimization problem is solved via standard first-order methods for modern DL (e.g., (adaptive) gradient methods). When  $\mathbf{x}$  contains multiple components with

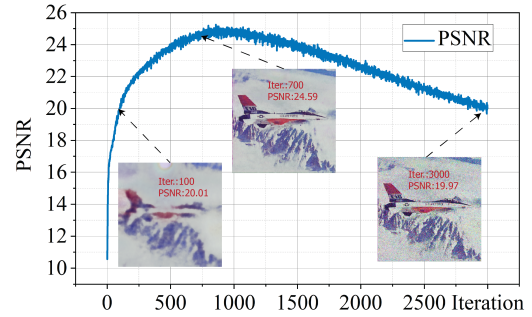


**Fig. 1** The early-learning-then-overfitting (ELTO) phenomenon in DIP for image denoising. The quality of the estimated image climbs to a peak first and then plunges once noise is picked up by the model  $G_{\theta}(\mathbf{z})$  also.

different physical meanings, one can naturally parametrize  $\mathbf{x}$  using multiple DNNs.

The simple procedure has produced surprisingly competitive recovery results on a myriad of visual IPs, from low-level image denoising, super-resolution, inpainting (Heckel & Hand, 2018; J. Liu, Sun, Xu, & Kamilov, 2018; Ulyanov et al., 2018) and blind deconvolution (Asim, Shamshad, & Ahmed, 2019; Ren, Zhang, Wang, Hu, & Zuo, 2020; Tran, Tran, Phung, & Hoai, 2021; Wang, Wang, Li, & Bilen, 2019), to mid-level image decomposition (Gandelsman, Shocher, & Irani, 2019) and image fusion (Ma, Hill, & Achim, 2021), and to advanced computational imaging problems (Baguer, Leuschner, & Schmidt, 2020; Cascarano, Sebastiani, Comes, Franchini, & Porta, 2021; Darestani & Heckel, 2021; Gong, Catana, Qi, & Li, 2021; Hand, Leong, & Voroninski, 2018; Hashimoto & Ote, 2021; Tayal et al., 2021; Veen et al., 2020; Williams et al., 2019; Yoo et al., 2021) (see the survey Qayyum et al. (2021)). A salient feature of the procedure is *no extra training data*, despite the presence of DNNs: the  $G_{\theta}$ ’s—often convolutional neural networks (CNNs)—are chosen to simply enforce structural priors for natural visual objects.

## 1.2 Overfitting issue in DIP

A critical detail that we have glossed over above is *overfitting*. Since  $G_{\theta}$  is substantially overparameterized,  $G_{\theta}(\mathbf{z})$  can in principle represent arbitrary elements in the  $\mathbf{x}$  domain. Globally optimizing (2) would normally lead to  $\mathbf{y} = f(G_{\theta}(\mathbf{z}))$ , but a priori the reconstruction  $G_{\theta}(\mathbf{z})$  may not reproduce  $\mathbf{x}$ , e.g., when  $f$  is non-injective, or  $\mathbf{y} \approx f(\mathbf{x})$

so that  $G_{\theta}(\mathbf{z})$  also accounts for modeling and observational noise.

Fortunately, the combination of DIP models and first-order optimization methods offers a blessing: in practice,  $G_{\theta}(\mathbf{z})$  has a bias toward the desired visual content, and learns it much faster than learning the noise. So the reconstruction quality climbs to a peak before potential degradation due to noise; see Fig. 1. This “early-learning-then-overfitting” (ELTO) phenomenon has been repeatedly reported in prior works, and is also backed by theories on simple  $G_{\theta}$  and linear  $f$  (Heckel & Soltanolkotabi, 2020a, 2020b). The successes of DIP models claimed above are mostly conditioned on the premise that appropriate *early stopping* (ES) around the performance peak can be made.

### 1.3 Prior work addressing the overfitting

Without the groundtruth  $\mathbf{x}$ , we cannot compute the performance curve as shown in Fig. 1. To resolve the overfitting issue, one can possibly resort to visual inspection, but this quickly becomes infeasible for many scenarios, such as (1) large-scale batch processing, (2) recovery of visual contents tricky to be visualized and/or examined by eyes (e.g., 3D or 4D visual objects), and (3) scientific imaging of unfamiliar objects (e.g., MRI imaging of rare tumors, and microscopic imaging of new virus species). Overall, there are mainly three lines of algorithm developments to counter the overfitting.

- **Regularization:** Heckel and Hand (2018) mitigates overfitting by restricting the size of  $G_{\theta}$  to the underparameterized regime. Cheng, Gadelha, Maji, and Sheldon (2019b); Jo, Chun, and Choi (2021); Metzler, Mousavi, Heckel, and Baraniuk (2018); Shi, Mettes, Maji, and Snoek (2021) control the network capacity by regularizing the norms of layerwise weights or the network Jacobian of  $G_{\theta}$ . Cascarano et al. (2021); J. Liu et al. (2018); Mataev, Milanfar, and Elad (2019); Sun (2021) use additional regularizer(s)  $R(G_{\theta}(\mathbf{z}))$ , such as total-variation norm or trained denoisers, to favor “simple” reconstructions. However, in general it is difficult to choose the right regularization level to preserve the peak performance while avoiding overfitting,

and the optimal  $\lambda$  likely depends on the noisy type and level, as shown in Section 3.1—the default  $\lambda$ ’s for selected methods in this category still lead to overfitting for high-level noise.

- **Noise modeling:** You, Zhu, Qu, and Ma (2020) models sparse additive noise as an explicit term in their optimization objective. Jo et al. (2021) designs Gaussian- and shot-specific regularizers and ES criteria. Ding, Jiang, Chen, Qu, and Zhu (2021) explores subgradient methods with diminishing step-size schedules for impulse noise with the  $\ell_1$  loss, with preliminary success. These methods do not work beyond the noise types and levels they target, whereas our knowledge about the noise in a given visual object is typically limited.
- **Early stopping (ES):** Very recently, several works perform ES directly. Shi et al. (2021) tracks the progress based on a ratio of no-reference blurriness and sharpness, but the criterion only works for their modified DIP models, as knowledge by the authors and confirmed in Section 3.1. Jo et al. (2021) provides noise-specific regularizer and ES criterion as alluded to above, but it is unclear how to extend the methods to unknown noise types and levels. Most close to the current work is Li et al. (2021), from a subset of the current authors. There, we propose monitoring the DIP reconstruction quality by training a coupled autoencoder. Although it leads to similar detection performance to the method we propose below, the extra autoencoder training slows down the whole process dramatically; see Section 3. Ding et al. (2021) effectively also performs ES, where the iteration stalls when the step size becomes negligible.

### 1.4 Our contribution

In this paper, we advocate the ES approach for practicality reasons: (1) The regularization and noise modeling approaches, even if effective, often do not improve the peak performance but push it until the last iterations; there could be  $\geq 10\times$  more iterations spent than that of climbing to the peak in the original DIP models; (2) Both approaches operate on the basis of deep or even precise knowledge about the noise type and level, which is practically unknown for most applications. If their key models and hyperparameters are

not set appropriately, overfitting likely remains. Then one still needs to perform ES.

We propose a novel ES criterion for DIP models by simply tracking the trend of the running variance of the reconstruction sequence. Our ES method is

- **Effective:** The gap between our detected and the peak performance, i.e., detection gap, is typically very small, as measured by standard visual quality metrics (PSNR: peak signal-to-noise ratio, and SSIM: structural similarity index measure);
- **Efficient:** It is lightweight, and the per-iteration overhead is at most a fraction of—the standard version in Algorithm 1, or even negligible relative to—the variant in Algorithm 2, the per-iteration cost of optimizing problem (2);
- **General:** Our method works well for DIP and its variants, including deep decoder (Heckel & Hand, 2018, DD) and sinusoidal representation networks (Sitzmann, Martel, Bergman, Lindell, & Wetzstein, 2020, SIREN), different noise types and levels, and across a number of visual IPs. Also, our method can be wrapped around several regularization methods, e.g., Gaussian process-DIP (Cheng, Gadelha, Maji, & Sheldon, 2019a, GP-DIP), DIP with total variation regularization (Cascarano et al., 2021; J. Liu et al., 2018, DIP-TV) to perform reasonable ES when they fail to prevent overfitting.
- **Robust:** Our method is relatively insensitive to the two hyperparameters, i.e., window size and patience number (see Sections 2 and 3.5). By contrast, the hyperparameters of most methods we reviewed above are sensitive to the noise type and level.

## 2 Our Early-Stopping (ES) Method

We assume this basic setup:  $\mathbf{x}$  is the groundtruth visual object of size  $N$  but unknown to us. We observe the variable sequence  $\{\boldsymbol{\theta}^t\}_{t \geq 1}$ , and the corresponding reconstruction sequence  $\{\mathbf{x}^t\}_{t \geq 1}$ , where  $\mathbf{x}^t \doteq G_{\boldsymbol{\theta}^t}(\mathbf{z})$ . By default, the performance is measured in terms of peak signal-to-noise ratio

(PSNR): for any  $\mathbf{x}'$ ,

$$\text{PNSR}(\mathbf{x}') = 10 \log_{10} \frac{\|\mathbf{x}\|_{\infty}^2}{\text{MSE}(\mathbf{x}')}, \quad (3)$$

where  $\|\mathbf{x}\|_{\infty}$  takes the largest magnitude in  $\mathbf{x}$ , and the mean squared error  $\text{MSE}(\mathbf{x}') = \|\mathbf{x} - \mathbf{x}'\|_F^2/N$ .

### 2.1 More details on major ES methods

Here, we provide more details on major competing methods, all of them ES-based except for You et al. (2020).

Shi et al. (2021) operates on DD models, and proposes two modifications to change the spectral bias: (1) controlling the operator norm of the weight  $\mathbf{w}$  for each convolutional layer by the normalization

$$\mathbf{w}' = \frac{\mathbf{w}}{\max(1, \|\mathbf{w}\|_{\text{op}}/\lambda)}, \quad (4)$$

ensuring that  $\|\mathbf{w}'\|_{\text{op}} \leq \lambda$ , which in turn controls the Fourier spectrum of the underlying function represented by the layer; (2) performing Gaussian upsampling instead of the typical bilinear upsampling to suppress the smoothness effect of the latter. These two modifications with appropriate parameter setting ( $\lambda$ , and  $\sigma$  in Gaussian filtering) can improve the learning of the high-frequency components by DD, and allow the blurriness-over-sharpness stopping criterion

$$\Delta r(\mathbf{x}^t) = \frac{1}{W} \left| \sum_{w=1}^W r(\mathbf{x}^{t-w}) - \sum_{w=1}^W r(\mathbf{x}^{t-W-w}) \right|, \quad (5)$$

where  $r(\mathbf{x}') = B(\mathbf{x}')/S(\mathbf{x}')$ , and  $B(\cdot)$  and  $S(\cdot)$  are the blurriness and sharpness metrics in Crete, Dolmieri, Ladret, and Nicolas (2007) and Bahrami and Kot (2014), respectively. In other words, the criterion in Eq. (5) measures the change of average blurriness-over-sharpness ratios over consecutive windows of size  $W$ , and small changes indicate good ES points. But, as said, this criterion only works for the modified DD models and not other DIP variants, as acknowledged by the authors in Shi et al. (2021) and confirmed in our experiment (see Section 3.1.4).



Jo et al. (2021) targets Gaussian denoising with known noise levels (i.e.,  $\mathbf{y} = \mathbf{x} + \mathbf{n}$ , where  $\mathbf{n}$  is iid Gaussian noise), and considers the objective

$$\min_{\theta} \frac{1}{n^2} \|\mathbf{y} - G_{\theta}(\mathbf{y})\|_F^2 + \frac{\sigma^2}{n^2} \text{tr } \mathbf{J}_{G_{\theta}}(\mathbf{y}), \quad (6)$$

where  $\text{tr } \mathbf{J}_{G_{\theta}}(\mathbf{y})$  is the trace of the network Jacobian with respect to the input, i.e., the divergence term in Jo et al. (2021). The divergence term is a proxy for controlling the capacity of the network. The paper then proposes a heuristic zero-crossing stopping criterion that stops the iteration when the loss starts to cross zero into negative values. Although the idea works reasonably well on Gaussian denoising with low and known noise level (the variance level  $\sigma^2$  is explicitly needed in the regularization parameter ahead of the divergence term), it starts to break down when the noise level increases even if the right noise level is provided; see Section 3.1.3. Also, although the paper has extended the formulation to handle Poisson noise, it is unclear how to generalize the idea for handling other types of noise, as well as how to move beyond simple additive denoising problems.

Our previous work Li et al. (2021) proposes training an autoencoder online using the reconstruction sequence  $\{\mathbf{x}^t\}_{t \geq 1}$ :

$$\min_{\mathbf{w}, \mathbf{v}} \sum_{t \geq 1} \ell_{\text{AE}}(\mathbf{x}^t, D_{\mathbf{w}} \circ E_{\mathbf{v}}(\mathbf{x}^t)). \quad (7)$$

Any new  $\mathbf{x}^t$  is passed through the current autoencoder, and the reconstruction error  $\ell_{\text{AE}}$  is recorded. We observe that the error curve typically follows a U-shape, and the valley of the curve is approximately aligned with the peak of the PSNR curve. We hence design an ES method by detecting the valley of the error curve. This method works reasonably well across different IPs and different DIP variants. A major drawback is the efficiency: the overhead caused by online training of the autoencoder is order-of-magnitude larger than the cost of DIP update itself, as shown in Section 3.4.

You et al. (2020) considers additive sparse (e.g., salt-and-pepper noise) noise only and proposes modeling the clean image and noise explicitly in the objective:

$$\min_{\theta, \mathbf{g}, \mathbf{h}} \|\mathbf{y} - G_{\theta}(\mathbf{z}) - (\mathbf{g} \circ \mathbf{g} - \mathbf{h} \circ \mathbf{h})\|_F^2, \quad (8)$$

where the overparametrized term  $\mathbf{g} \circ \mathbf{g} - \mathbf{h} \circ \mathbf{h}$  ( $\circ$  denotes the Hadamard product) is meant to capture the sparse noise, where a similar idea has proved effective for sparse recovery in Vaškevičius, Kanade, and Rebeschini (2019). Different properly-tuned learning rates for the clean image and sparse noise terms are necessary for success. The downside includes the prolonged running time as it pushes the peak reconstruction to the very last iteration, and the difficulty to extend the idea to other types of noise.

## 2.2 The MSE curve and intuition for our method

Since we do not know  $\mathbf{x}$ , we cannot access the PSNR curve or the corresponding MSE curve. But we observe that (Fig. 2) generally the MSE

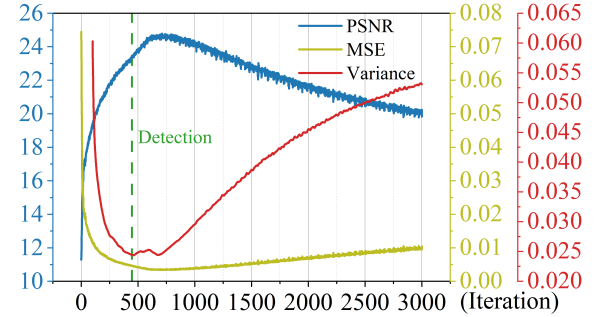


**Fig. 2** Relationship between the PSNR, MSE, and VAR curves. Our method relies on the VAR curve, whose valley is often well aligned with the MSE valley, to detect the MSE valley—that corresponds to the PSNR peak.

(resp. PSNR) curve follows a U (resp. bell) shape:  $\|\mathbf{x}^t - \mathbf{x}\|$  initially drops quickly to a low level, and then climbs back due to the noise effect. This is the ELTO phenomenon we discussed in Section 1; we hope to detect the valley of this U-shaped MSE curve.

How to gauge the shape of the MSE curve without knowing  $\mathbf{x}$ ? We consider the running variance (VAR):

$$\text{VAR}(t) \doteq \frac{1}{W} \sum_{w=0}^{W-1} \|\mathbf{x}^{t+w} - \frac{1}{W} \sum_{i=0}^{W-1} \mathbf{x}^{t+i}\|_F^2. \quad (9)$$

In the initial stage, the models quickly learns the desired visual content, as reflected by the rapid climbing PSNR curve and the rapid diminishing

MSE curve (see Fig. 2). So we expect the running variance of  $\{\mathbf{x}^t\}_{t \geq 1}$  to drop quickly also, which is indeed the case as shown in Fig. 2. When the iteration is near the MSE valley, all the  $\mathbf{x}^t$ 's are near to but scattered around  $\mathbf{x}$ . So  $\frac{1}{W} \sum_{i=0}^{W-1} \mathbf{x}^{t+i} \approx \mathbf{x}$  and

$$\text{VAR}(t) \approx \frac{1}{W} \sum_{w=0}^{W-1} \|\mathbf{x}^{t+w} - \mathbf{x}\|_F^2. \quad (10)$$

This argument suggests a U-shaped VAR curve also, and the curve should follow the high-level trend of the MSE curve, particularly the two with aligned valleys. Our ES method hence tries to detect the valley of the VAR curve as recommended stopping point.

Similar to Shi et al. (2021), our paper also relies on certain running statistics of the  $\{\mathbf{x}^t\}$  sequence. However, our running variance is much easier to compute, and more critically, works well across a number of different tasks and DIP variants, as shown in Figs. 3 and 4, and Section 3. Compared to our previous method in Li et al. (2021) that trains a coupled autoencoder online, the current method is much more lightweight. The competing methods Jo et al. (2021); You et al. (2020) deal with only particular types of noise in additive denoising problems only, and entail highly nontrivial modifications to DIP formulations.

## 2.3 Detecting transition by running variance

Our lightweight computation only involves calculating the VAR curve, and numerically detecting the valley of the VAR curve. To calculate the variance, we set a window size parameter  $W$  and compute the windowed moving variance (WMV). To robustly detect the valley, we introduce a patience number  $P$  to tolerate up to  $P$  consecutive steps of variance stagnation. Obviously, the cost is dominated by the variance calculation per step, which is  $O(WN)$  ( $N$  is the size of the visual object). In comparison, a typical gradient update step for solving Eq. (2) costs at least  $\Omega(|\theta|N)$ , where  $|\theta|$  is the number of parameters in the DNN  $G_\theta$ <sup>1</sup>. Since  $|\theta|$  is typically much larger than  $W$  (we

---

### Algorithm 1 DIP with ES-WMV

---

**Input:** random seed  $\mathbf{z}$ , randomly-initialized  $G_\theta$ , window size  $W$ , patience number  $P$ , empty queue  $\mathcal{Q}$ , iteration counter  $k = 0$ ,  $\text{VAR}_{\min} = \infty$

**Output:** reconstruction  $\mathbf{x}^*$

- 1: **while** not stopped **do**
- 2:   update  $\theta$  via Eq. (2) to obtain  $\theta^{k+1}$  and  $\mathbf{x}^{k+1}$
- 3:   push  $\mathbf{x}^{k+1}$  to  $\mathcal{Q}$ , pop queue if  $|\mathcal{Q}| > W$
- 4:   **if**  $|\mathcal{Q}| = W$  **then**
- 5:     compute VAR of elements in  $\mathcal{Q}$  via Eq. (9)
- 6:     **if**  $\text{VAR} < \text{VAR}_{\min}$  **then**
- 7:        $\text{VAR}_{\min} \leftarrow \text{VAR}$ ,  $\mathbf{x}^* \leftarrow \mathbf{x}^{k+1}$
- 8:     **end if**
- 9:   **end if**
- 10:   **if**  $\text{VAR}_{\min}$  stagnates for  $P$  iterations **then**
- 11:     stop and return  $\mathbf{x}^*$
- 12:   **end if**
- 13:    $k = k + 1$
- 14: **end while**

---

set the default value to 100), our running VAR and detection induce very little computational overhead.

Our whole algorithmic pipeline is summarized in Algorithm 1. To confirm the effectiveness, we provide sample qualitative results in Figs. 3 and 4, with more quantitative results included in the experiment part (Section 3). Fig. 3 shows on image denoising with different types and levels of noise, our ES method can detect near-peak ES points. Similarly, our method remains effective on several popular DIP variants, as shown in Fig. 4.

## 2.4 Partial theoretical justification

We can make our heuristic argument in Section 2.2 slightly more rigorous by restricting ourselves to additive denoising, i.e.,  $\mathbf{y} = \mathbf{x} + \mathbf{n}$ , and appealing to the popular linearization strategy (i.e., neural tangent kernel Heckel and Soltanolkotabi (2020b); Jacot, Gabriel, and Hongler (2018)) in

---

<sup>1</sup>To see this, consider a simple formulation for additive denoising:  $\min_{\theta} \|\mathbf{y} - G_\theta(\mathbf{z})\|_F^2$ , where we assume  $G_\theta(\mathbf{z})$  is

---

the DIP model so that: 1)  $\mathbf{z}$  is the same size as the output visual object; and 2) the layers are typical convolutional layers. Obviously, a forward pass to compute the function value costs at least  $\Omega(|\theta|N)$ , and the backward pass in back-propagation costs a small constant times that of the forward pass.

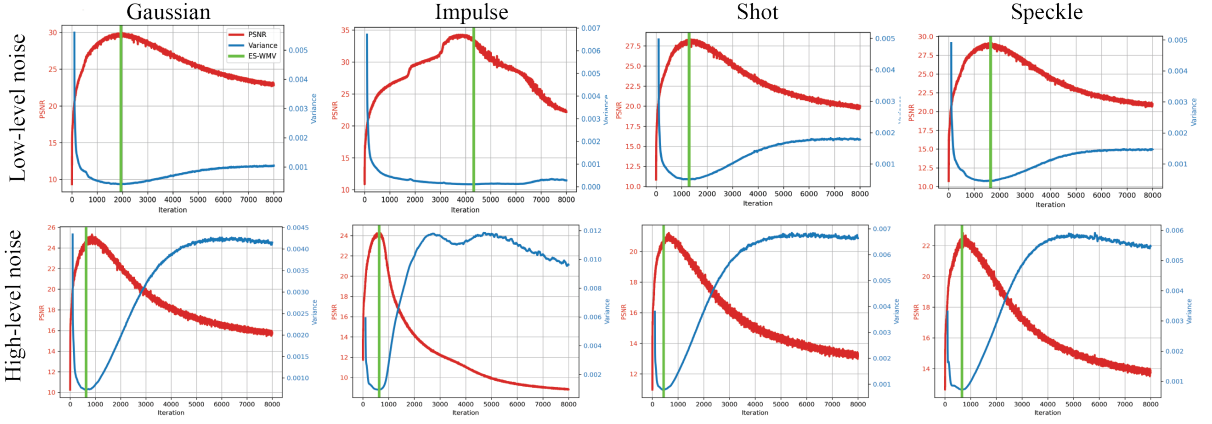


**Fig. 3** Our ES-WMV method on DIP for denoising “F16” with different noise types and levels (top: low-level noise; bottom: high-level noise). Red curves are PSNR curves, and blue curves are VAR curves. The green bars indicate the detected ES point.

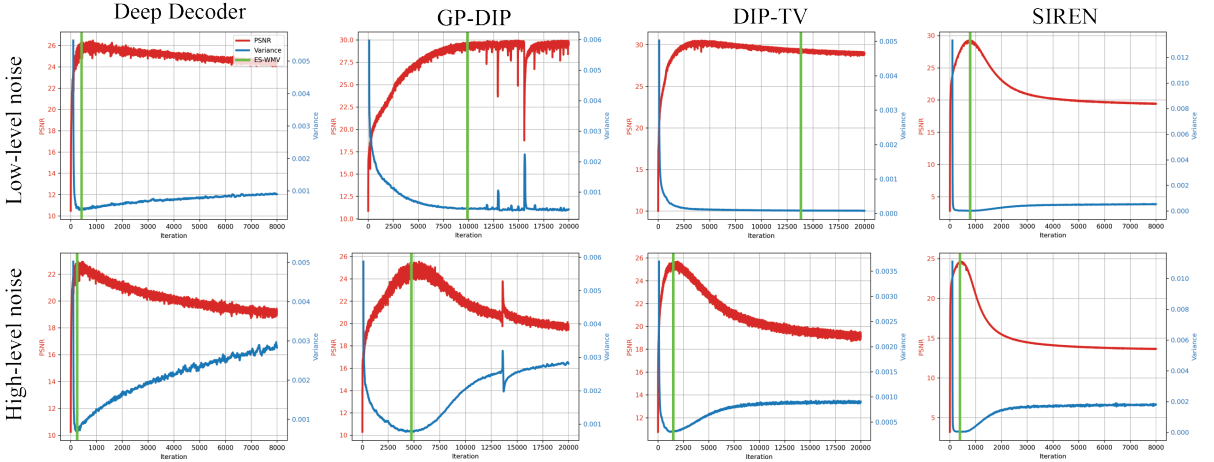


**Fig. 4** Our ES-WMV method on DD, GP-DIP, DIP-TV, and SIREN for denoising “F16” with different levels of Gaussian noise (top: low-level noise; bottom: high-level noise). Red curves are PSNR curves, and blue curves are VAR curves. The green bars indicate the detected ES point.

understanding DNNs. The idea is based on the assumption that during DNN training  $\theta$  does not move much from initialization  $\theta^0$ , so that the learning dynamic can be approximated by that of a linearized model, i.e., suppose we take the MSE loss

$$\begin{aligned} \|y - G_\theta(z)\|_2^2 &\approx \\ \|y - G_{\theta^0}(z) - J_G(\theta^0)(\theta - \theta^0)\|_2^2 &\doteq \hat{f}(\theta), \end{aligned} \quad (11)$$

where  $J_G(\theta^0)$  is the Jacobian of  $G$  with respect to  $\theta$  at  $\theta^0$ , and  $G_{\theta^0}(z) + J_G(\theta^0)(\theta - \theta^0)$  is the

first-order Taylor approximation to  $G_\theta(z)$  around  $\theta^0$ .  $\hat{f}(\theta)$  is simply a least-squares objective. We can directly calculate the running variance based on the linear model, as shown below.

**Theorem 2.1** *Let  $\sigma_i$ ’s and  $w_i$ ’s be the singular values and left singular vectors of  $J_G(\theta^0)$ , and suppose we run gradient descent with step size  $\eta$  on the linearized objective  $\hat{f}(\theta)$  to obtain  $\{\theta^t\}$  and  $\{x^t\}$  with  $x^t \doteq G_{\theta^0}(z) + J_G(\theta^0)(\theta^t - \theta^0)$ . Then provided that  $\eta \leq 1/\max_i(\sigma_i^2)$ , the running variance of  $\{x^t\}$  is*

$$\text{VAR}(t) = \sum_i C_{m,\eta,\sigma_i} \langle w_i, \hat{y} \rangle^2 \left(1 - \eta \sigma_i^2\right)^{2t}, \quad (12)$$

where  $\hat{\mathbf{y}} = \mathbf{y} - G_{\theta^0}(\mathbf{z})$ , and  $C_{W,\eta,\sigma_i} \geq 0$  only depends on  $W$ ,  $\eta$ , and  $\sigma_i$  for all  $i$ .

The proof can be found in [Section A.1](#). [Theorem 2.1](#) shows that if the learning rate (LR)  $\eta$  is sufficiently small, the WMV of  $\{\mathbf{x}^t\}$  is monotonically decreasing. The result correctly predicts the initial trend, but conflicts with the climbing trend after the performance peak. This is a common limitation of the current linearization-based deep learning theory ([Chizat, Oyallon, & Bach, 2018](#); [C. Liu, Zhu, & Belkin, 2020](#)), as the late-stage learning dynamic may deviate substantially from that of the linearized version. Another factor is that practical LR is not very small.

We can develop an upper bound for the WMV that does have a U shape, with the caveat that this is only an upper bound. To this end, we make use of Theorem 1 of [Heckel and Soltanolkotabi \(2020b\)](#), which can be summarized (some technical details omitted; precise statement reproduced in [Section A.2](#)) as follows: consider two-layer model  $G_C(\mathbf{B}) = \text{ReLU}(\mathbf{U}\mathbf{B}\mathbf{C})\mathbf{v}$ , where  $\mathbf{C} \in \mathbb{R}^{n \times k}$  models  $1 \times 1$  trainable convolutions,  $\mathbf{v} \in \mathbb{R}^{k \times 1}$  contains fixed weights,  $\mathbf{U}$  is an upsampling operation, and  $\mathbf{B}$  is the fixed random seed. Let  $\mathbf{J}$  be a reference Jacobian matrix solely determined by the upsampling operation  $\mathbf{U}$ , and  $\sigma_i$ 's and  $\mathbf{w}_i$ 's the singular values and left singular vectors of  $\mathbf{J}$ . Assume  $\mathbf{x} \in \text{span}\{\mathbf{w}_1, \dots, \mathbf{w}_p\}$ . Then when  $\eta$  is sufficiently small, with high probability,

$$\|G_{C^t}(\mathbf{B}) - \mathbf{x}\|_2 \leq (1 - \eta\sigma_p^2)^t \|\mathbf{x}\|_2 + E(\mathbf{n}) + \varepsilon\|\mathbf{y}\|_2,$$

where  $\varepsilon > 0$  is a small scalar related to the structure of the network and  $E(\mathbf{n})$  is the error introduced by noise:  $E^2(\mathbf{n}) \doteq \sum_{j=1}^n ((1 - \eta\sigma_j^2)^t - 1)^2 \langle \mathbf{w}_j, \mathbf{n} \rangle^2$ . So if the gap  $\sigma_p/\sigma_{p+1} > 1$ ,  $\|G_{C^t}(\mathbf{B}) - \mathbf{x}\|_2$  is dominated by  $(1 - \eta\sigma_p^2)^t \|\mathbf{x}\|_2$  when  $t$  is small, and then by  $E(\mathbf{n})$  when  $t$  is large. But since the former decreases and the latter increases when  $t$  grows, the upper bound has a U shape with respect to  $t$ . Based on this result, we have:

**Theorem 2.2** *Assume the same setting as Theorem 2 of [Heckel and Soltanolkotabi \(2020b\)](#). Our WMV is upper bounded by*

$$\frac{12}{W} \|\mathbf{x}\|_2^2 \frac{(1 - \eta\sigma_p^2)^{2t}}{1 - (1 - \eta\sigma_p^2)^2} + 12 \sum_{i=1}^n \left( (1 - \eta\sigma_i^2)^{t+W-1} - 1 \right)^2 (\mathbf{w}_i^T \mathbf{n})^2 + 12\varepsilon^2 \|\mathbf{y}\|_2^2.$$

with high probability.

The exact statement and proof can be found in [Section A.2](#). By similar reasoning as above, we can conclude that the upper bound in [Theorem 2.2](#) also has a U shape. To help interpret the results, [Fig. 5](#) shows the curves (as functions of  $t$ ) predicted by [Theorems 2.1](#) and [2.2](#). We reiterate that the exact calculation is conditioned on the validity of linearization, which is justified for the initial stage but not necessarily for the whole process. The actual VAR curve should lie between the two curves.

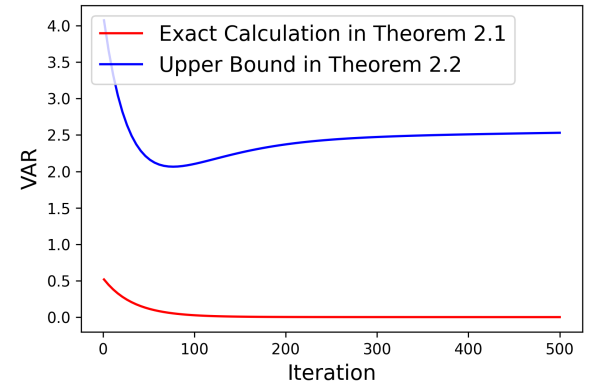


**Fig. 5** The exact and upper bounds predicted by [Theorems 2.1](#) and [2.2](#).

## 2.5 A memory-efficient variant

While [Algorithm 1](#) is already lightweight and effective in practice, we can slightly modify it to avoid maintaining the  $\mathbf{Q}$  and hence save memory. The trick is to use exponential moving variance (EMV), together with the calculation of exponential moving average (EMA). The hard window size parameter  $W$  is now replaced by the soft forgetting factor  $\alpha$ : larger the  $\alpha$ , smaller the impact of the history and hence a smaller effective window.

**Algorithm 2** DIP with ES-EMV

---

**Input:** random seed  $\mathbf{z}$ , randomly-initialized  $G_{\theta}$ , forgetting factor  $\alpha \in (0, 1)$ , patience number  $P$ , iteration counter  $k = 0$ ,  $\text{EMA}^0 = 0$ ,  $\text{EMV}^0 = 0$ ,  $\text{VAR}_{\min} = \infty$

**Output:** reconstruction  $\mathbf{x}^*$

```

1: while not stopped do
2:   update  $\theta$  via Eq. (2) to obtain  $\theta^{k+1}$  and  $\mathbf{x}^{k+1}$ 
3:    $\text{EMA}^{k+1} = (1 - \alpha)\text{EMA}^k + \alpha\mathbf{x}^{k+1}$ 
4:    $\text{EMV}^{k+1} = (1 - \alpha)\text{EMV}^k + \alpha(1 - \alpha)\|\mathbf{x}^{k+1} - \text{EMA}^k\|_2^2$ 
5:   if  $\text{VAR} < \text{VAR}_{\min}$  then
6:      $\text{VAR}_{\min} \leftarrow \text{VAR}$ ,  $\mathbf{x}^* \leftarrow \mathbf{x}^{k+1}$ 
7:   end if
8:   if  $\text{VAR}_{\min}$  stagnates for  $P$  iterations then
9:     stop and return  $\mathbf{x}^*$ 
10:  end if
11:   $k = k + 1$ 
12: end while

```

---

### 3 Experiments

We test our variance-based ES method (ES-WMV) on 3 families of visual IPs: image denoising, MRI reconstruction, and blind image deblurring, spanning both linear and nonlinear IPs. For image denoising, we also systematically evaluate ES-WMV on major variants of DIP that try to mitigate overfitting, including DD (Heckel & Hand, 2018)<sup>2</sup>, DIP-TV (Cascarano et al., 2021)<sup>3</sup>, GP-DIP (Cheng et al., 2019b)<sup>4</sup>, and demonstrate ES-WMV as a reliable helper to detect good ES points, whether these methods succeed or not in removing the overfitting. We also compare ES-WMV with major competing methods, including SB (Shi et al., 2021)<sup>5</sup>, DF-STE (Jo et al., 2021)<sup>6</sup>, SV-ES (Li et al., 2021)<sup>7</sup> and DOP (You et al., 2020)<sup>8</sup>.

Our default setup for all experiments is as follows. Our DIP model is the original one

from Ulyanov et al. (2018)<sup>9</sup>; the optimizer is ADAM with a learning rate 0.01. For all other models, we use their default architectures, optimizers, and hyperparameters. For ES-WMV, the default window size  $W = 100$ , and patience number  $P = 1000$ . We use both PSNR and SSIM to access the reconstruction quality, and we report PSNR and SSIM gaps (difference between our detected and peak numbers) as an indicator of our detection performance. For most experiments, we repeat the experiments 3 times to report the mean and standard deviation; when not, we explain why.

#### 3.1 Image denoising

Prior works dealing with the DIP overfitting issue mostly focus on image denoising, but typically only evaluate their methods on one or two kinds of noise with low noise levels, e.g., low-level Gaussian noise. Here, to stretch out the evaluation, we consider 4 types of noise: Gaussian, shot, impulse, and speckle. We take the classic 9-image dataset<sup>10</sup>, and for each noise type generate two noise levels, low and high, i.e., level 2 and level 4 of Hendrycks and Dietterich (2019), respectively.

##### 3.1.1 Noise generation

Following the noise generation rules of Hendrycks and Dietterich (2019)<sup>11</sup>, we simulate four kinds of noise and three intensity levels for each noise type. The detailed information is as follows.

- **Gaussian noise:** 0 mean additive Gaussian noise with variance 0.12, 0.18, and 0.26 for low, medium, and high noise levels, respectively;
- **Impulse noise:** also known as salt-and-pepper noise, replacing each pixel with probability  $p \in [0, 1]$  into white or black pixel with half chance each. Low, medium, and high noise levels correspond to  $p = 0.3, 0.5, 0.7$ , respectively;
- **Speckle noise:** for each pixel  $x \in [0, 1]$ , the noisy pixel is  $x(1 + \varepsilon)$ , where  $\varepsilon$  is 0-mean Gaussian with a variance level 0.20, 0.35, 0.45 for low, medium, and high noise levels, respectively;
- **Shot noise:** also known as Poisson noise. For each pixel  $x \in [0, 1]$ , the noisy pixel is Poisson

---

<sup>2</sup>[https://github.com/reinhardt/supplement\\_deep\\_decoder](https://github.com/reinhardt/supplement_deep_decoder)

<sup>3</sup><https://github.com/sedaboni/ADMM-DIPTV>

<sup>4</sup><https://people.cs.umass.edu/~zezhoucheng/gp-dip/>

<sup>5</sup><https://github.com/shizenglin/Measure-and-Control-Spectral-Bias>

<sup>6</sup><https://github.com/gistvision/dip-denoising>

<sup>7</sup><https://github.com/sun-umn/Self-Validation>

<sup>8</sup><https://github.com/ChongYou/robust-image-recovery>

---

<sup>9</sup><https://github.com/DmitryUlyanov/deep-image-prior>

<sup>10</sup>[http://www.cs.tut.fi/~foi/GCF-BM3D/index.html#ref\\_results](http://www.cs.tut.fi/~foi/GCF-BM3D/index.html#ref_results)

<sup>11</sup><https://github.com/hendrycks/robustness>



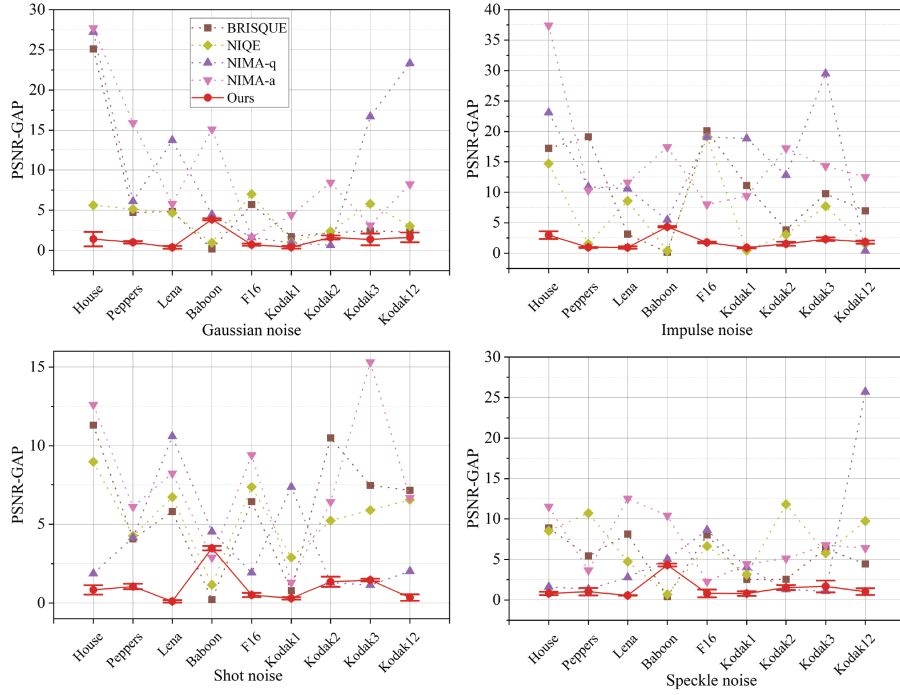


**Fig. 6** Low-level noise detection performance in terms of PSNR gaps. For NIMA, we report both technical quality assessment (NIMA-q) and aesthetic assessment (NIMA-a). Smaller PSNR gaps are better.

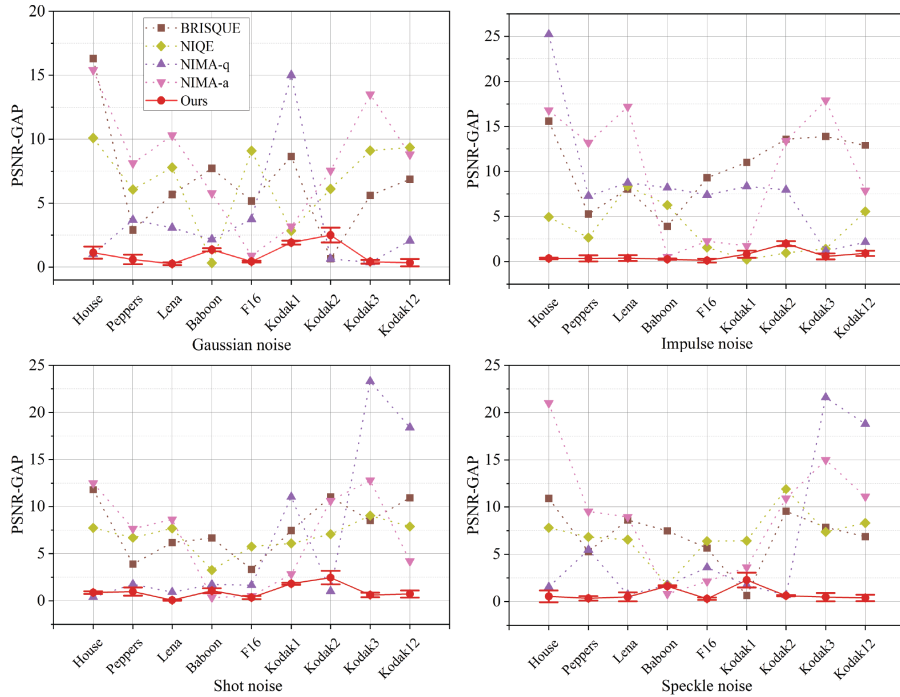


**Fig. 7** High-level noise detection performance in terms of PSNR gaps. For NIMA, we report both technical quality assessment (NIMA-q) and aesthetic assessment (NIMA-a). Smaller PSNR gaps are better.

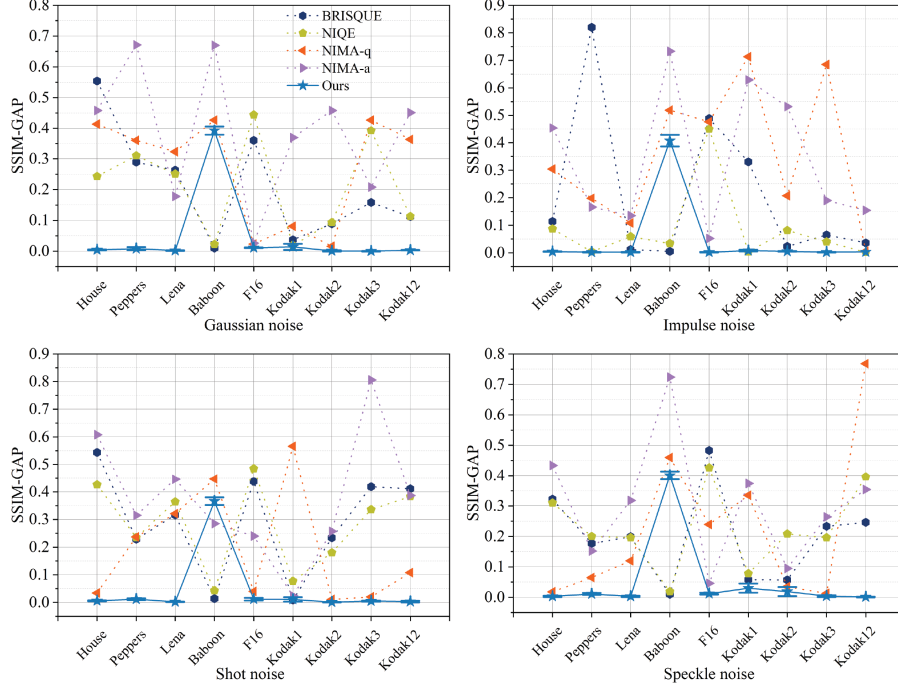


**Fig. 8** Low-level noise detection performance in terms of SSIM gaps. For NIMA, we report both technical quality assessment (NIMA-q) and aesthetic assessment (NIMA-a). Smaller SSIM gaps are better.

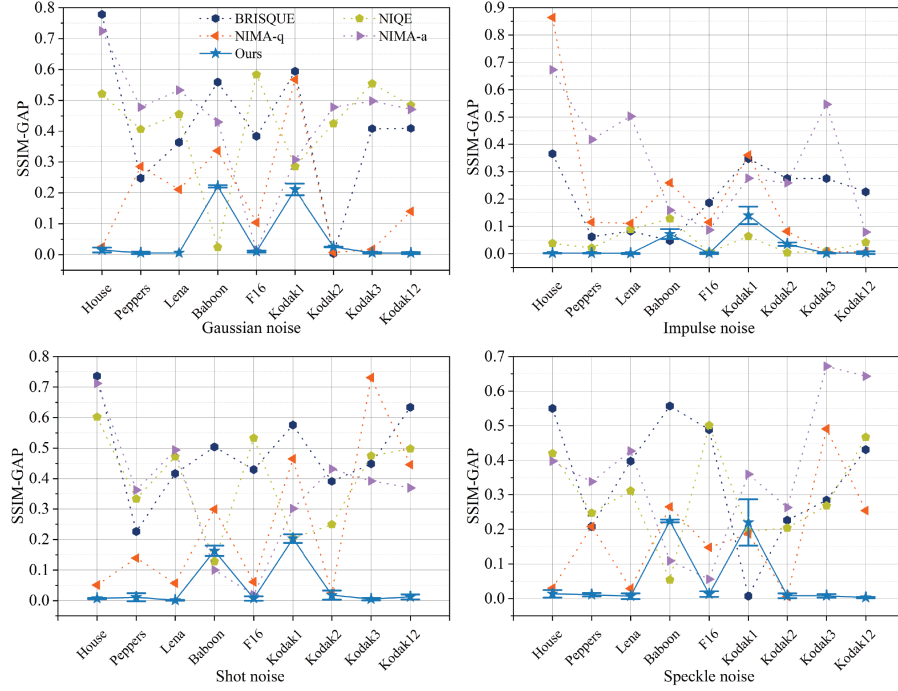


**Fig. 9** High-level noise detection performance in terms of SSIM gaps. For NIMA, we report both technical quality assessment (NIMA-q) and aesthetic assessment (NIMA-a). Smaller SSIM gaps are better.

distributed with rate  $\lambda x$ , where  $\lambda$  is 25, 12, 5 for low, medium, and high noise levels, respectively.

### 3.1.2 Comparison with baseline methods

It is natural to expect that no-reference image quality assessment (NR-IQA), such as the classic BRISQUE (Mittal, Moorthy, & Bovik, 2012), NIQE (Mittal, Soundararajan, & Bovik, 2012) or state-of-the-art (SOTA) DNN-based NIMA (Talebi & Milanfar, 2018) can possibly make good ES criteria. We thus set up a family of baseline methods, using each of these metrics to find optimal stopping.

The comparison between ES-WMV and these baseline methods for PSNR gaps is presented in Figs. 6 and 7, for low- and high-level noise level, respectively. While our method enjoys favorable detection gaps ( $\leq 2$ ) for most tested noise types and levels (except for Baboon, Kodak1, Kodak2 for certain noise type/level; we suspect this is due to the substantial high-frequency components in these two images), detection gaps by the baseline methods can very often get huge  $\geq 10$ . We hence do not report the mean and standard deviation for these methods, as it is unlikely these bad detection results are due to randomness. In addition, we report the SSIM gaps of low- and high-level noise cases in Fig. 8 and Fig. 9, respectively, which show similar trend to the results of PSNR gaps. The detection gaps of our method are very marginal ( $< 0.02$ ) for most noise types and levels (except for Baboon and Kodak1 for certain noise type/level), while the baseline methods can well exceed 0.1 for most cases.

### 3.1.3 Comparison with competing methods

**Table 2** DIP with ES-WMV vs. DOP on impulse noise: mean and (std).

	Low Level		High Level	
	PSNR	SSIM	PSNR	SSIM
DIP-ES	31.64 (5.69)	0.85 (0.18)	24.74 (3.23)	0.67 (0.19)
DOP	32.12 (4.52)	0.92 (0.07)	27.34 (3.78)	0.86 (0.10)

We continue to compare our method with 4 main competitors: DF-STE, SV-ES, DOP, and SB.

DF-STE is specific for Gaussian and Poisson denoising, and the noise variance is needed for their tuning parameters. Figs. 10 and 11 present the comparison with DF-STE. Here, we directly report the final PSNRs and SSIMs obtained by both methods<sup>12</sup>. For low-noise level, there is no clear winner. For high-noise level, ES-WMV outperforms DF-STE by considerable margins, i.e., detection lines of ES-WMV are above those of DF-STE for most of the cases. We stress that the right variance level is provided to DF-STE in order to tune their regularization parameters, but DF-STE stops after only very few epochs leading to the very low performance and almost zero standard deviations—they return almost the noisy input. However, we do not perform any parameter tuning for ES-WMV.

SV-ES is designed to work for all noise types and levels. We report the results in Fig. 12; ES-WMV performs largely comparably to SV-ES. However, ES-WMV enjoys obvious benefits in terms of wall-clock time, shown in Table 5: for each epoch, the overheads of our ES-WMV are less than 3/4 of the DIP update itself, while SV-ES is around 25 $\times$  of that. There is no surprise: while our method only needs to update the running variance of the reconstruction in each epoch, SV-ES needs to perform one round of forward- and backward passes of the autoencoder which is much more expensive.

DOP is designed specifically for impulse noise, and hence we compare ES-WMV with DOP only on denoising impulse noise (Table 2). The loss is changed to  $\ell_1$  to account for the sparsity of the noise. In terms of the final PSNRs, DOP outperforms ES-WMV by a small gap. We note that the peak PSNR of DIP with  $\ell_1$  lags behind DOP by about 2 points for high noise levels.

For SB, our test first confirms that the stopping criterion as defined in Eq. (5) fails on the original DIP for Gaussian denoising; in particular, their performance is sensitive to their stopping threshold; see Fig. 13. Moreover, the modified DIP model in Shi et al. (2021) still suffers from the

<sup>12</sup>A technical detail we need to clarify here is: in DF-STE Jo et al. (2021), when they add Gaussian or shot noise to the images, they do not perform clipping to make sure the pixel values remain in the range  $[0, 255]$ . This is not physical, and this kind of saturation is a serious type of practical noise. Following Hendrycks and Dietterich (2019), we perform clipping in the data.

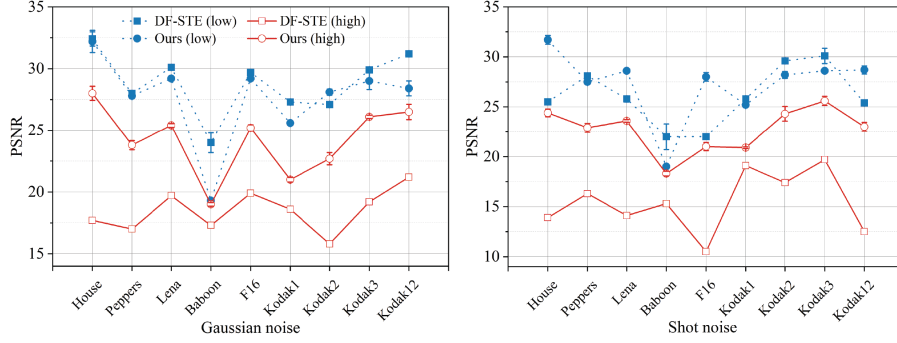


**Fig. 10** Comparison of DF-STE and ES-WMV for Gaussian and shot noise in terms of PSNR.

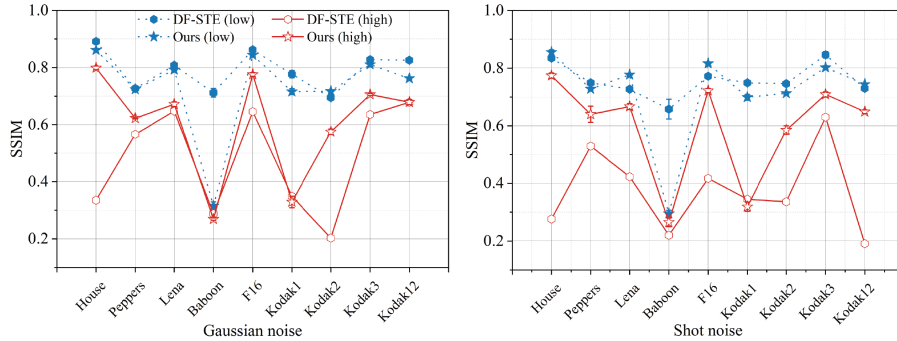


**Fig. 11** Comparison of DF-STE and ES-WMV for Gaussian and shot noise in terms of SSIM.

**Table 3** Comparison between ES-WMV and SB for image denoising on the CBSD68 dataset with varying noise level  $\sigma$ . Higher detected PSNR and earlier detection are better, which are in **red**: mean and (std).

	$\sigma = 15$		$\sigma = 25$		$\sigma = 50$	
	PSNR	Epoch	PSNR	Epoch	PSNR	Epoch
WMV	28.7(3.2)	<b>3962</b> (2506)	<b>27.4</b> (2.6)	<b>3068</b> (2150)	<b>24.2</b> (2.3)	<b>1548</b> (1939)
SB	<b>29.0</b> (3.1)	4908(1757)	27.3(2.2)	5099(1776)	23.0(1.0)	5765(1346)

overfitting issue beyond the very low noise levels that the paper has tested on, as shown in Fig. 14, at least when the key parameters  $\lambda$  and  $\sigma$  are not properly tuned—this is a common issue for methods that try to use regularization to remove the overfitting issue. Their proposed ES method does not stop at appropriately places when the noise level is high. To support these points, we test both ES-WMV and SB on the modified DIP model in Shi et al. (2021), based on two datasets (as is done in their paper): the classic 9-image dataset (Dabov, Foi, Katkovnik, & Egiazarian, 2007) and the CBSD68 dataset (Martin, Fowlkes, Tal, & Malik, 2001). Part of the qualitative detection results on the 9 images are shown in Fig. 14; detected PSNR and stopping epochs of on the

CBSD68 dataset are reported in Table 3. For SB, the detection threshold parameter is fixed at 0.01. It is evident that both methods have similar detection performance for low noise levels but ES-WMV outperforms SB when the noise level is high. Moreover, ES-WMV tends to stop much earlier than SB, saving the computational cost.

### 3.1.4 ES-WMV as a helper

DD, DIP+TV, GP-DIP represent different regularization strategies for controlling overfitting. A critical and challenging problem, however, is setting the right hyperparameters for them so that overfitting is removed while peak-level performance is preserved. So practically, these methods are not free from overfitting, especially when the noise level is high. Thus, instead of treating them as competitors, we here test if ES-WMV can reliably detect good ES points for them. We focus on Gaussian denoising, and report the results in Fig. 15 (a)-(c) and Fig. 16 (a)-(c). ES-WMV is able to attain  $\leq 1$  PSNR gap for most of the cases, with few outliers. These regularizations typically

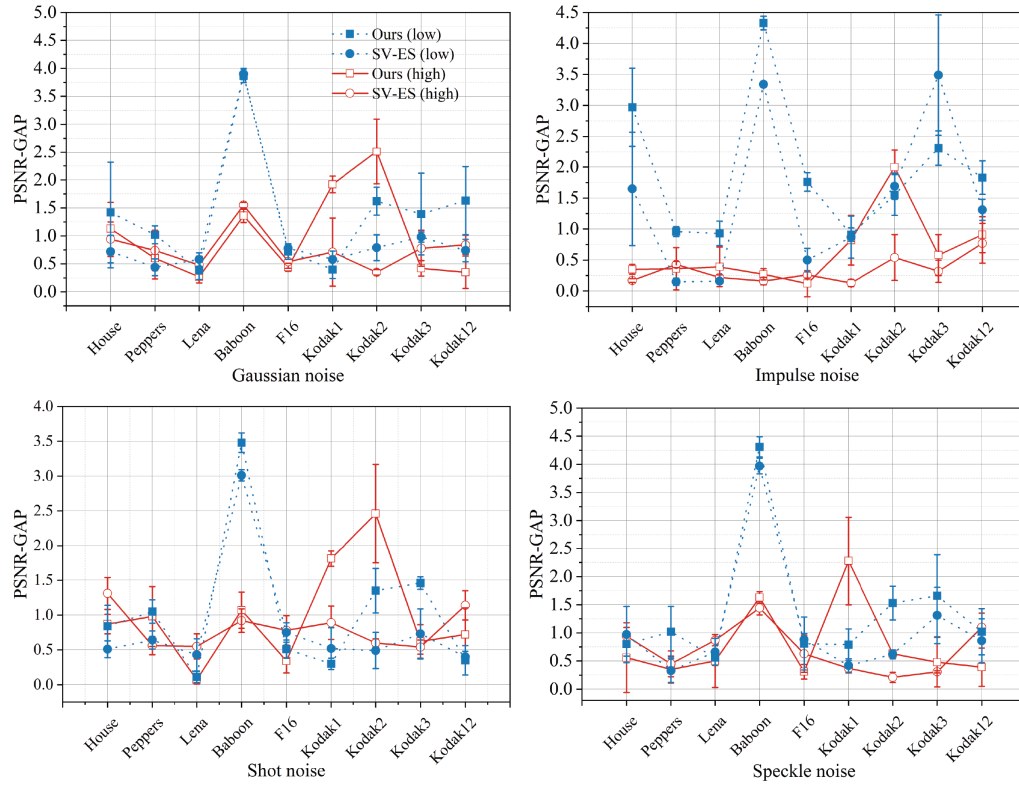


**Fig. 12** Low- and high- level noise detection performance of SV-ES and ours in terms of PSNR gaps.

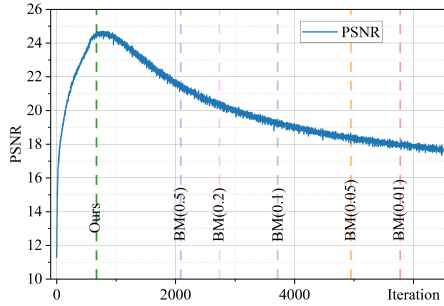


**Fig. 13** Comparison of SB and ES-WMV for DIP ES detection. While our ES-WMV can reliably detect a near-peak performance level, it is hard to set appropriately stopping parameter for the SB metric. In fact, the original paper [Shi et al. \(2021\)](#) acknowledges that SB does not work for the original DIP model.

change the recovery trajectory. We suspect that finetuning of our method may improve on these corner cases—we leave this as future research.

SIREN ([Sitzmann et al., 2020](#)) is a relative of DIP models, but parameterizes  $\mathbf{x}$  as the discretization of a continuous function: this function

takes into spatial coordinates and returns the corresponding function values. This parameterization proves beneficial in representing visual objects with substantial high-frequency components, compared to typical CNNs models used in DIP. In this experiment, we test SIREN as a replacement of DIP models for Gaussian denoising, and summarize the results in [Fig. 15 \(d\)](#) and [Fig. 16 \(d\)](#). ES-WMV is again able to detect near-peak performance for most images.

### 3.1.5 Performance on real-world denoising

As stated from the beginning, ES-WMV is designed with real-world IPs in mind, targeting unknown noise types and levels. Given the encouraging performance above, we test it on the standard RGB track of NTIRE 2020 Real Image Denoising Challenge ([Abdelhamed et al., 2020](#)). Just to be clear, our purpose here is not to compete with SOTA methods on this dataset—they are data-driven methods based on the training set provided in the challenge, or to prove the



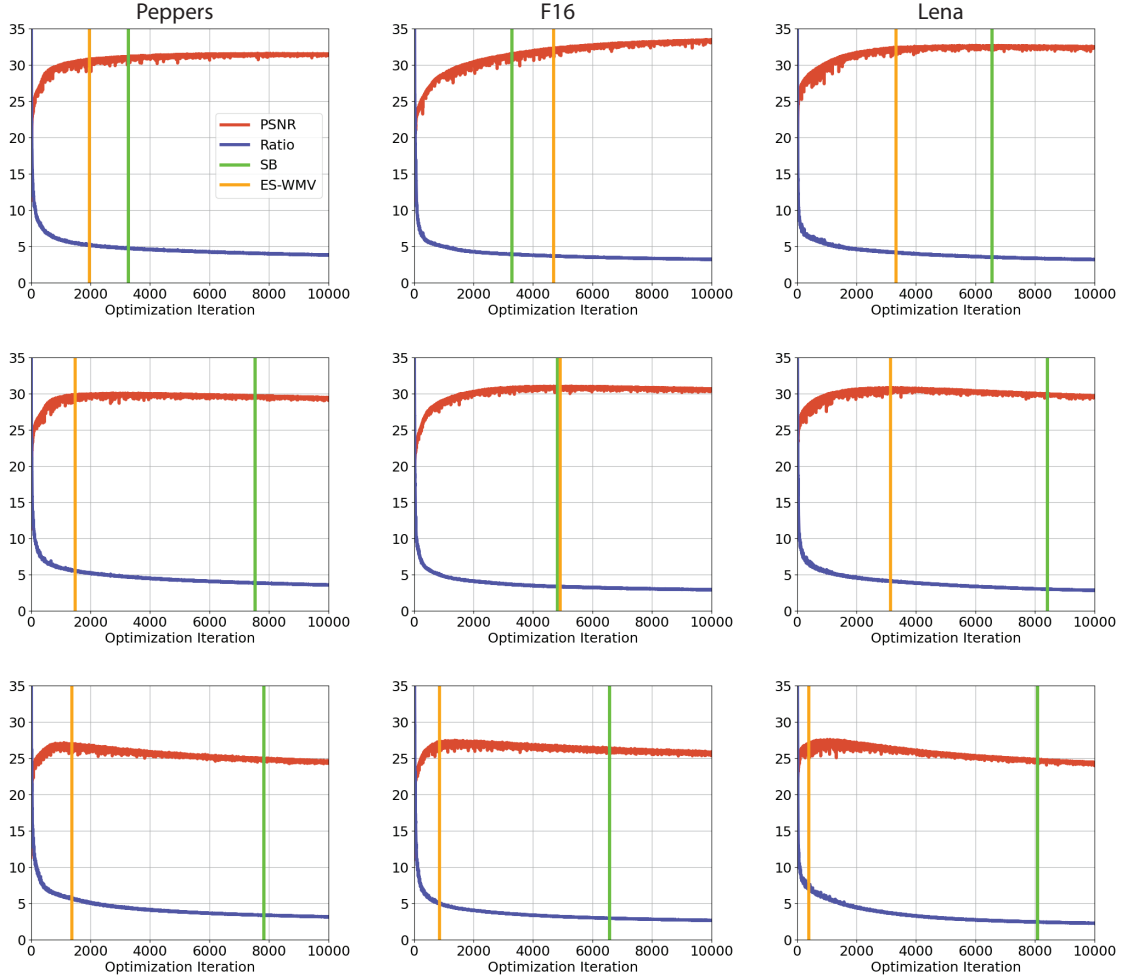


**Fig. 14** Comparison between ES-WMV and SB for image denoising (top:  $\sigma = 15$ ; middle:  $\sigma = 25$ ; bottom:  $\sigma = 50$ ). The red and blue curves are the PSNR and the ratio metric (defined in Eq. (5)) curves. The orange and green bars indicate the ES points detected by our ES-WMV and SB, respectively.

supremacy of DIP for denoising. We simply focus on evaluating ES-WMV in a real-world setting. So we directly test ES-WMV on the validation dataset, which comprises 1024 images of size  $256 \times 256$ . Since the noise types and levels are unknown, we try both MSE, as well as the more robust  $\ell_1$  and Huber losses. The results are reported in

**Table 4** DIP with ES-WMV on real image denoising: mean and (std).

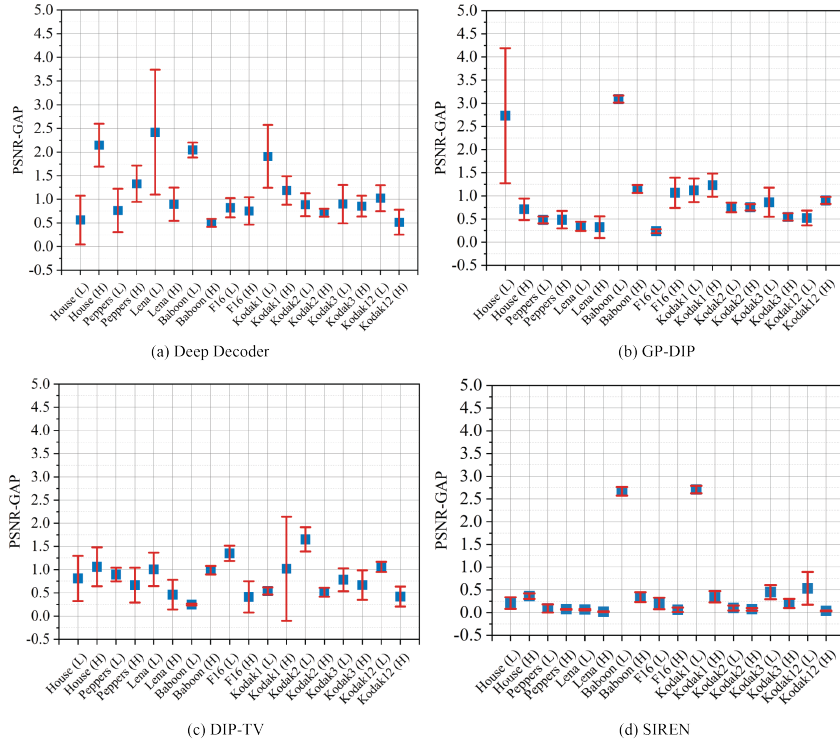
	PSNR	PSNR Gap	SSIM	SSIM Gap
DIP (MSE)	34.04 (3.68)	0.92 (0.83)	0.92 (0.07)	0.02 (0.04)
DIP ( $\ell_1$ )	33.92 (4.34)	0.92 (0.59)	0.93 (0.05)	0.02 (0.02)
DIP (Huber)	33.72 (3.86)	0.95 (0.73)	0.92 (0.06)	0.02 (0.03)

Table 4. We do not repeat the experiments here;

the means and standard deviations are obtained over the 1024 images. Our detection gaps are mostly  $\leq 1.7$  in PSNR and  $\leq 0.06$  in SSIM, even slightly better than the above results on the simulated data. Also, the absolute PSNR and SSIM detected are surprisingly high, and the MSE loss outperforms the robust losses, strongly suggesting the noise level in the dataset may be relatively low.

### 3.2 MRI reconstruction

We now test ES-WMV on MRI reconstruction, a classical linear IP with a nontrivial forward mapping:  $\mathbf{y} \approx \mathcal{F}(x)$ , where  $\mathcal{F}$  is the subsampled Fourier operator, and we use  $\approx$  to indicate the noise encountered in practical MRI imaging



**Fig. 15** Performance of ES-WMV on DD, GP-DIP, DIP-TV, and SIREN for Gaussian denoising in terms of PSNR gaps. L: low noise level; H: high noise level

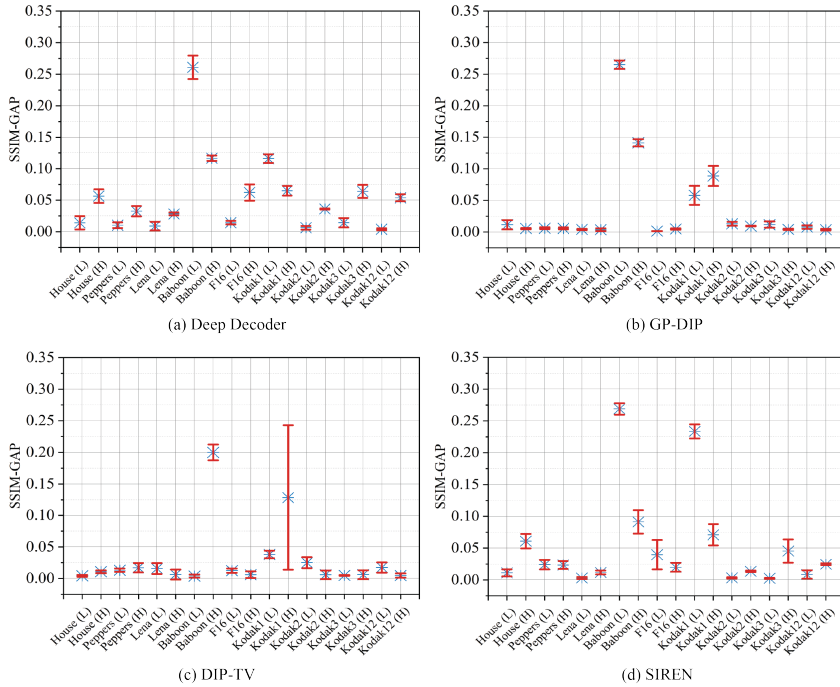


**Fig. 16** Performance of ES-WMV on DD, GP-DIP, DIP-TV, and SIREN for Gaussian denoising in terms of SSIM gaps. L: low noise level; H: high noise level

may be hybrid (e.g., additive, shot) and uncertain. Here, we take 8-fold undersampling, and parametrize  $\mathbf{x}$  using “Conv-Decoder” (Darestani & Heckel, 2021), a variant of DD. Due to the heavy overparameterization, overfitting occurs and ES is needed. Darestani and Heckel (2021) directly set the stopping point at the 2500-th epoch, and we run our ES-WMV. We pick two random cases (C1: 1001339 and C2: 1000190) from Darestani and Heckel (2021), which are part of the same fastMRI dataset (Zbontar et al., 2018). Fig. 17 reports the detection performance (quality measured in SSIM only, to be consistent with Darestani and Heckel (2021)).

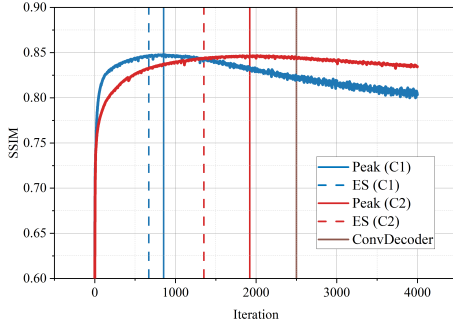


**Fig. 17** Detection performance on MRI reconstruction

It is clear that ES-WMV detects near-performance for both cases, and it is adaptive enough to yield comparable or better ES points than heuristically fixing the ES point as done in ConvDecoder.

### 3.3 Blind image deblurring (BID)

In BID, a blurry and noisy image is given, and the goal is to recover a sharp and clean image. The blur is mostly caused by motion and/or optical nonideality in the camera, and the forward process is often modeled as  $\mathbf{y} = \mathbf{k} * \mathbf{x} + \mathbf{n}$ , where  $\mathbf{k}$  is blur kernel,  $\mathbf{n}$  models additive sensory noise, and  $*$  is linear convolution to model the spatial uniformity of the blur effect (Szeliski, 2021). BID is a very challenging visual IP due to the bilinearity:  $(\mathbf{k}, \mathbf{x}) \mapsto \mathbf{k} * \mathbf{x}$ . Recently, Asim et al. (2019); Ren et al. (2020); Tran et al. (2021); Wang et al. (2019) have tried to use DIP models to solve BID

by modeling  $\mathbf{k}$  and  $\mathbf{x}$  as two separate DNNs, i.e.,

$$\min_{\theta_k, \theta_x} \|\mathbf{y} - G_{\theta_k}(\mathbf{z}_k) * G_{\theta_x}(\mathbf{z}_x)\|_2^2 + \lambda \frac{\|\nabla G_{\theta_x}(\mathbf{z}_x)\|_1}{\|\nabla G_{\theta_x}(\mathbf{z}_x)\|_2},$$

where the regularizer is to promote sparsity in the gradient domain for the reconstruction of  $\mathbf{x}$ , as is standard in BID. Here, we follow Ren et al. (2020) and choose multi-layer perceptron (MLP) with softmax activation for  $G_{\theta_k}$ , and the canonical DIP model (CNN-based encoder-decoder architecture) for  $G_{\theta_x}(\mathbf{z}_x)$ . We change their regularizer from the original  $\|\nabla G_{\theta_x}(\mathbf{z}_x)\|_1$  to the current, as their original formulation is tested only on a very low noise level,  $\sigma = 10^{-5}$  and no overfitting is observed. We set to work with higher noise level  $\sigma = 10^{-3}$ , and we find that their original formulation does not work for high-level noise. The positive effect of the modified regularizer on BID has been reported before (Krishnan, Tay, & Fergus, 2011). We have a forthcoming paper Zhuang, Li, Wang, and Sun (2022) studying these ideas more comprehensively.

For our experiment, we take 4 images and 3 kernels from the standard Levin dataset (Levin, Weiss, Durand, & Freeman, 2011), resulting in 12 image-kernel combinations. The high noise level leads to substantial overfitting, as shown in Fig. 18 (top). Nonetheless, ES-WMV can reliably detect good ES points and lead to impressive visual reconstructions (see Fig. 18 (bottom)). Fig. 18 (middle) shows that our method returns quantitatively near-peak performance, far better than leaving the process to overfit.

### 3.4 ES-WMV vs. ES-EMV

We now consider our memory-efficient version (ES-EMV) as described in Algorithm 2, and compare it with ES-WMV, as shown in Fig. 19. Besides the memory benefit, ES-EMV runs around 100 times faster than ES-WMV, as reported in Table 5 and does seem to provide consistent improvement on the detected PSNRs, due to the strong smoothing effect (we set  $\alpha = 0.1$ ). For this paper, we prefer to stay simple and leave systematic evaluations of these variants as future work.

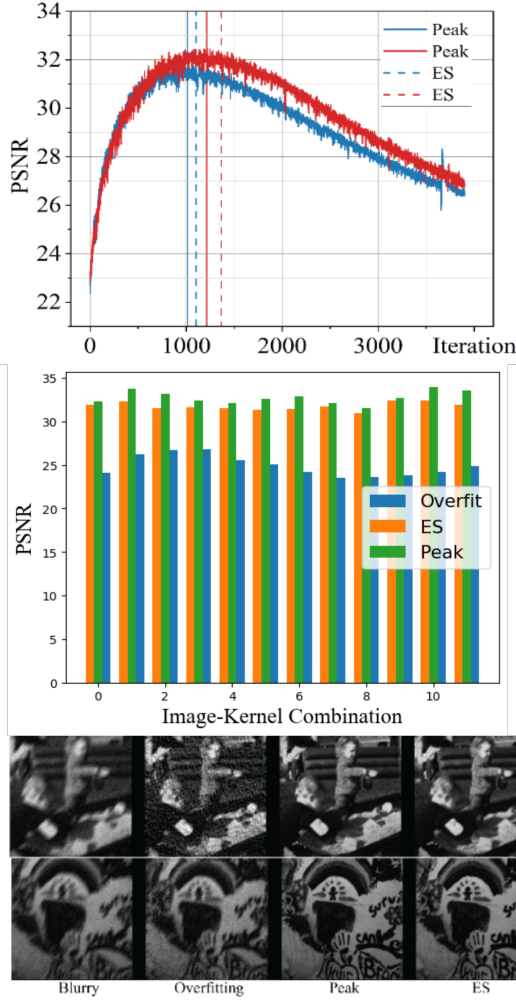


**Fig. 18** BID results (top: Example detection results on BID; middle: Quantitative detection results on 12 image-kernel combinations; bottom: Example recovered images)

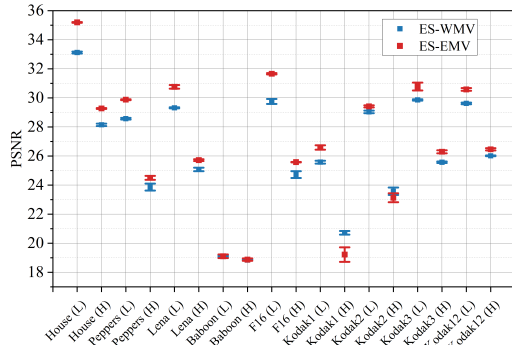


**Fig. 19** Detected PSNR comparison between ES-WMV and ES-EMV

**Table 5** Wall-clock time of DIP, SV-ES, ES-WMV and ES-EMV per epoch on *NVIDIA Tesla K40 GPU*: mean and (std).

	DIP	SV-ES	ES-WMV	ES-EMV
Time(secs)	0.448 (0.030)	13.027 (3.872)	0.301 (0.016)	0.003 (0.003)

### 3.5 Ablation study

The window size  $W$  (default 100) and patience number  $P$  (default: 1000) are the only hyperparameters for ES-WMV. To study their impact on ES detection, we vary them across a range and check how the detection gap changes for Gaussian denoising with medium-level noise, as shown in Fig. 20 and Fig. 21. Our method is quite robust against these changes, and it seems larger  $W$  and  $P$  can bring in marginal improvement to the performance.

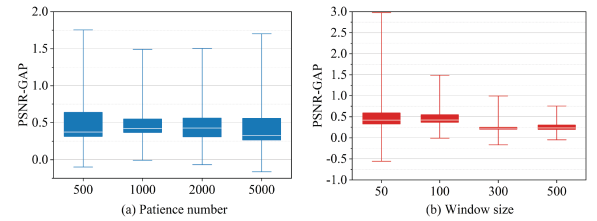


**Fig. 20** Effect of patience number and window size on detection in terms of PSNR gaps

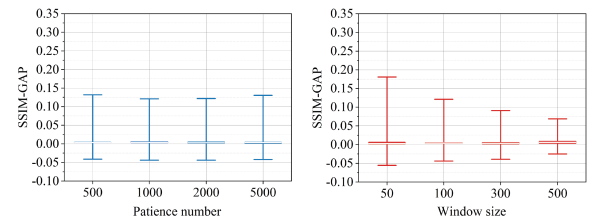


**Fig. 21** Effect of patience number and window size on detection in terms of SSIM gaps

## 4 Discussion

We have proposed a simple yet effective ES detection method (ES-WMV, and the ES-EMV variant) that seems to work robustly across multiple visual IPs and DIP variants. In comparison, some competing ES methods are noise- or DIP-model-specific, and only work for limited scenarios; our

previous ES method [Li et al. \(2021\)](#) has comparable performance but it slows down the running speed too much.

Our ES method struggles with images with substantial high-frequency components. Addressing this likely requires refining the DIP models. Our theoretical justification is only partial, sharing the same difficulty of analyzing DNNs in general.

Besides ES, there are other major technical barriers to make DIP models practical and competitive for visual IPs. A major thing is efficiency: one needs to train a DNN using iterative methods for every instance, and there is also no natural way of performing smart initialization on  $\theta$ , even if a decent  $x$  is provided.

## Acknowledgement

Zhong Zhuang, Hengkang Wang, Tiancong Chen, and Ju Sun are partly supported by NSF CMMI 2038403. The authors acknowledge the Minnesota Supercomputing Institute (MSI) at the University of Minnesota for providing resources that contributed to the research results reported within this paper.



## Appendix A

### A.1 Proof of Theorem 2.1

*Proof* To simplify the notation, we write  $\hat{\mathbf{y}} \doteq \mathbf{y} - G_{\theta^0}(\mathbf{z})$ ,  $\mathbf{J} \doteq \mathbf{J}_G(\theta^0)$ , and  $\mathbf{c} \doteq \theta - \theta^0$ . So the least-squares objective in Eq. (11) is equivalent to

$$\|\hat{\mathbf{y}} - \mathbf{J}\mathbf{c}\|_2^2 \quad (\text{A1})$$

and the gradient update reads

$$\mathbf{c}^t = \mathbf{c}^{t-1} - \eta \mathbf{J}^\top (\mathbf{J}\mathbf{c}^{t-1} - \hat{\mathbf{y}}), \quad (\text{A2})$$

where  $\mathbf{c}^0 = \mathbf{0}$  and  $\mathbf{x}^t = \mathbf{J}\mathbf{c}^t + G_{\theta^0}(\mathbf{z})$ . The residual at time  $t$  can be computed as

$$\mathbf{r}^t \doteq \hat{\mathbf{y}} - \mathbf{J}\mathbf{c}^t \quad (\text{A3})$$

$$= \hat{\mathbf{y}} - \mathbf{J} \left( \mathbf{c}^{t-1} - \eta \mathbf{J}^\top (\mathbf{J}\mathbf{c}^{t-1} - \hat{\mathbf{y}}) \right) \quad (\text{A4})$$

$$= (\mathbf{I} - \eta \mathbf{J}\mathbf{J}^\top) (\hat{\mathbf{y}} - \mathbf{J}\mathbf{c}^{t-1}) \quad (\text{A5})$$

$$= (\mathbf{I} - \eta \mathbf{J}\mathbf{J}^\top)^2 (\hat{\mathbf{y}} - \mathbf{J}\mathbf{c}^{t-2}) = \dots \quad (\text{A6})$$

$$= (\mathbf{I} - \eta \mathbf{J}\mathbf{J}^\top)^t (\hat{\mathbf{y}} - \mathbf{J}\mathbf{c}^0) \quad (\text{using } \mathbf{c}^0 = \mathbf{0}) \quad (\text{A7})$$

$$= (\mathbf{I} - \eta \mathbf{J}\mathbf{J}^\top)^t \hat{\mathbf{y}}. \quad (\text{A8})$$

Assume the SVD of  $\mathbf{J}$  as  $\mathbf{J} = \mathbf{W}\Sigma\mathbf{V}^\top$ . Then

$$\mathbf{r}^t = (\mathbf{I} - \eta \mathbf{W}\Sigma^2\mathbf{W}^\top)^t \hat{\mathbf{y}} = \sum_i \left(1 - \eta\sigma_i^2\right)^t \mathbf{w}_i^\top \hat{\mathbf{y}} \mathbf{w}_i \quad (\text{A9})$$

and so

$$\mathbf{J}\mathbf{c}^t = \hat{\mathbf{y}} - \mathbf{r}^t = \sum_i \left(1 - \left(1 - \eta\sigma_i^2\right)^t\right) \mathbf{w}_i^\top \hat{\mathbf{y}} \mathbf{w}_i. \quad (\text{A10})$$

Consider a set of  $W$  vectors  $\mathcal{V} = \{\mathbf{v}_1, \dots, \mathbf{v}_W\}$ . We have that the empirical variance

$$\text{VAR}(\mathcal{V}) = \frac{1}{W} \sum_{w=1}^W \left\| \mathbf{v}_w - \frac{1}{W} \sum_{j=1}^W \mathbf{v}_j \right\|_2^2 = \frac{1}{W} \sum_{w=1}^W \|\mathbf{v}_w\|_2^2 - \left\| \frac{1}{W} \sum_{w=1}^W \mathbf{v}_w \right\|_2^2. \quad (\text{A11})$$

So the variance of the set  $\{\mathbf{x}^t, \mathbf{x}^{t+1}, \dots, \mathbf{x}^{t+W-1}\}$ , same as the variance of the set  $\{\mathbf{J}\mathbf{c}^t, \mathbf{J}\mathbf{c}^{t+1}, \dots, \mathbf{J}\mathbf{c}^{t+W-1}\}$ , can be calculated as

$$\frac{1}{W} \sum_{w=0}^{W-1} \sum_i (\mathbf{w}_i^\top \hat{\mathbf{y}})^2 \left(1 - (1 - \eta\sigma_i^2)^{t+w}\right)^2 - \frac{1}{W^2} \sum_i (\mathbf{w}_i^\top \hat{\mathbf{y}})^2 \left(\sum_{w=0}^{W-1} 1 - (1 - \eta\sigma_i^2)^{t+w}\right)^2 \quad (\text{A12})$$

$$= \frac{1}{W^2} \sum_i (\mathbf{w}_i^\top \hat{\mathbf{y}})^2 \left[ W \sum_{w=0}^{W-1} \left(1 - (1 - \eta\sigma_i^2)^{t+w}\right)^2 - \left(\sum_{w=0}^{W-1} 1 - (1 - \eta\sigma_i^2)^{t+w}\right)^2 \right] \quad (\text{A13})$$

$$= \frac{1}{W^2} \sum_i (\mathbf{w}_i^\top \hat{\mathbf{y}})^2 \left[ \left( W^2 + W \frac{(1 - \eta\sigma_i^2)^{2t} (1 - (1 - \eta\sigma_i^2)^{2W})}{1 - (1 - \eta\sigma_i^2)^2} - 2W \frac{(1 - \eta\sigma_i^2)^t (1 - (1 - \eta\sigma_i^2)^W)}{\eta\sigma_i^2} \right) \right. \\ \left. - \left( W^2 - 2W \frac{(1 - \eta\sigma_i^2)^t (1 - (1 - \eta\sigma_i^2)^W)}{\eta\sigma_i^2} + \frac{(1 - \eta\sigma_i^2)^{2t} \left(1 - (1 - \eta\sigma_i^2)^W\right)^2}{\eta^2 \sigma_i^4} \right) \right] \quad (\text{A14})$$

$$= \frac{1}{W^2} \sum_i \langle \mathbf{w}_i, \hat{\mathbf{y}} \rangle^2 \frac{(1 - \eta\sigma_i^2)^{2t}}{\eta\sigma_i^2} \left[ W \frac{1 - (1 - \eta\sigma_i^2)^{2W}}{2 - \eta\sigma_i^2} - \frac{(1 - (1 - \eta\sigma_i^2)^W)^2}{\eta\sigma_i^2} \right]. \quad (\text{A15})$$

So the constants  $C_{W,\eta,\sigma_i}$ 's are defined as

$$C_{W,\eta,\sigma_i} \doteq \frac{1}{W^2\eta\sigma_i^2} \left[ W \frac{1 - (1 - \eta\sigma_i^2)^{2W}}{2 - \eta\sigma_i^2} - \frac{(1 - (1 - \eta\sigma_i^2)^W)^2}{\eta\sigma_i^2} \right]. \quad (\text{A16})$$

To see they are nonnegative, it is sufficient to show that

$$W \frac{1 - (1 - \eta\sigma_i^2)^{2W}}{2 - \eta\sigma_i^2} - \frac{(1 - (1 - \eta\sigma_i^2)^W)^2}{\eta\sigma_i^2} \geq 0 \iff \eta\sigma_i^2 W (1 - (1 - \eta\sigma_i^2)^{2W}) - (2 - \eta\sigma_i^2)(1 - (1 - \eta\sigma_i^2)^W)^2 \geq 0.$$

Now consider the function

$$h(\xi, W) = \xi W (1 - (1 - \xi)^{2W}) - (2 - \xi)(1 - (1 - \xi)^W)^2 \quad \xi \in [0, 1], W \geq 1. \quad (\text{A17})$$

First, one can easily check that  $\partial_W h(\xi, W) \geq 0$  for all  $W \geq 1$  and all  $\xi \in [0, 1]$ , i.e.,  $h(\xi, W)$  is monotonically increasing with respect to  $W$ . Thus, in order to prove  $C_{W,\eta,\sigma_i} \geq 0$ , it suffices to show that  $h(\xi, 1) \geq 0$ . Now

$$h(\xi, 1) = \xi (1 - (1 - \xi)^2) - (2 - \xi)\xi^2 = 0, \quad (\text{A18})$$

completing the proof.  $\square$

## A.2 Proof of Theorem 2.2

We first restate Theorem 2 in Heckel and Soltanolkotabi (2020b).

**Theorem A.1** (Heckel and Soltanolkotabi (2020b)) *Let  $\mathbf{x} \in \mathbb{R}^n$  be a signal in the span of the first  $p$  trigonometric basis functions, and consider a noisy observation  $\mathbf{y} = \mathbf{x} + \mathbf{n}$ , where the noise  $\mathbf{n} \sim \mathcal{N}(\mathbf{0}, \xi^2/n \cdot \mathbf{I})$ . To denoise this signal, we fit a two-layer generator network  $G_{\mathbf{C}}(\mathbf{B}) = \text{ReLU}(\mathbf{U}\mathbf{B}\mathbf{C})\mathbf{v}$ , where  $\mathbf{v} = [1, \dots, 1, -1, \dots, -1]/\sqrt{k}$ , and  $\mathbf{B} \sim_{iid} \mathcal{N}(0, 1)$ , and  $\mathbf{U}$  is an upsampling operator that implements circular convolution with a given kernel  $\mathbf{u}$ . Denote  $\sigma \doteq \|\mathbf{u}\|_2 |\mathbf{F}g(\mathbf{u} \otimes \mathbf{u}/\|\mathbf{u}\|_2^2)|^{1/2}$  where  $g(t) = (1 - \cos^{-1}(t)/\pi)t$  and  $\otimes$  denotes the circular convolution. Fix any  $\varepsilon \in (0, \sigma_p/\sigma_1]$ , and suppose  $k \geq C_{\mathbf{u}}n/\varepsilon^8$ , where  $C_{\mathbf{u}} > 0$  is a constant only depending on  $\mathbf{u}$ . Consider gradient descent with step size  $\eta \leq \|\mathbf{F}\mathbf{u}\|_{\infty}^{-2}$  ( $\mathbf{F}\mathbf{u}$  is the Fourier transform of  $\mathbf{u}$ ) starting from  $\mathbf{C}_0 \sim_{iid} \mathcal{N}(0, \omega^2)$ , entries,  $\omega \propto \frac{\|\mathbf{y}\|_2}{\sqrt{n}}$ . Then, for all iterates  $t$  obeying  $t \leq \frac{100}{\eta\sigma_p^2}$ , the reconstruction error obeys*

$$\|G_{\mathbf{C}^t}(\mathbf{B}) - \mathbf{x}\|_2 \leq (1 - \eta\sigma_p^2)^t \|\mathbf{x}\|_2 + \sqrt{\sum_{i=1}^n ((1 - \eta\sigma_i^2)^t - 1)^2 (\mathbf{w}_i^T \mathbf{n})^2} + \varepsilon \|\mathbf{y}\|_2$$

with probability at least  $1 - \exp(-k^2) - n^{-2}$ .

Note that since  $\mathbf{B} \sim_{iid} \mathcal{N}(0, 1)$  and hence is full-rank with probability one, the original Theorem 1 & 2 of Heckel and Soltanolkotabi (2020b) rename  $\mathbf{B}\mathbf{C}$  into  $\mathbf{C}'$  and state the result directly on  $\mathbf{C}'$ , i.e., assume the model is  $\text{ReLU}(\mathbf{U}\mathbf{C}')\mathbf{v}$ . It is easy to see the original theorems imply the version stated here.

With this, we can obtain our Theorem 2.2, stated in full technical form here:

**Theorem A.2** *Let  $\mathbf{x} \in \mathbb{R}^n$  be a signal in the span of the first  $p$  trigonometric basis functions, and consider a noisy observation  $\mathbf{y} = \mathbf{x} + \mathbf{n}$ , where the noise  $\mathbf{n} \sim \mathcal{N}(\mathbf{0}, \xi^2/n \cdot \mathbf{I})$ . To denoise this signal, we fit a two-layer generator network  $G_{\mathbf{C}}(\mathbf{B}) = \text{ReLU}(\mathbf{U}\mathbf{B}\mathbf{C})\mathbf{v}$ , where  $\mathbf{v} = [1, \dots, 1, -1, \dots, -1]/\sqrt{k}$ , and  $\mathbf{B} \sim_{iid} \mathcal{N}(0, 1)$ , and  $\mathbf{U}$  is an upsampling operator that implements circular convolution with a given kernel  $\mathbf{u}$ . Denote  $\sigma \doteq \|\mathbf{u}\|_2 |\mathbf{F}g(\mathbf{u} \otimes \mathbf{u}/\|\mathbf{u}\|_2^2)|^{1/2}$  where  $g(t) = (1 - \cos^{-1}(t)/\pi)t$  and  $\otimes$  denotes the circular convolution. Fix any  $\varepsilon \in (0, \sigma_p/\sigma_1]$ , and suppose  $k \geq C_{\mathbf{u}}n/\varepsilon^8$ , where  $C_{\mathbf{u}} > 0$  is a constant only depending on  $\mathbf{u}$ . Consider gradient descent with step size*

$\eta \leq \|\mathbf{F}\mathbf{u}\|_\infty^{-2}$  ( $\mathbf{F}\mathbf{u}$  is the Fourier transform of  $\mathbf{u}$ ) starting from  $\mathbf{C}_0 \sim_{iid} \mathcal{N}(0, \omega^2)$ , entries,  $\omega \propto \frac{\|\mathbf{y}\|_2}{\sqrt{n}}$ . Then, for all iterates  $t$  obeying  $t \leq \frac{100}{\eta\sigma_p^2}$ , our WMV obeys

$$\text{WMV} \leq \frac{12}{W} \|\mathbf{x}\|_2^2 \frac{(1 - \eta\sigma_p^2)^{2t}}{1 - (1 - \eta\sigma_p^2)^2} + 12 \sum_{i=1}^n \left( (1 - \eta\sigma_i^2)^{t+W-1} - 1 \right)^2 (\mathbf{w}_i^\top \mathbf{n})^2 + 12\varepsilon^2 \|\mathbf{y}\|_2^2 \quad (\text{A19})$$

with probability at least  $1 - \exp(-k^2) - n^{-2}$ .

*Proof* We make use of the basic inequality:  $\|\mathbf{a} - \mathbf{b}\|_2^2 \leq 2\|\mathbf{a}\|_2^2 + 2\|\mathbf{b}\|_2^2$  for any two vectors  $\mathbf{a}, \mathbf{b}$  of compatible dimension. We have

$$\frac{1}{W} \sum_{w=0}^{W-1} \|G_{\mathbf{C}^{t+w}}(\mathbf{B}) - \frac{1}{W} \sum_{j=0}^{W-1} G_{\mathbf{C}^{t+j}}(\mathbf{B})\|_2^2 \quad (\text{A20})$$

$$= \frac{1}{W} \sum_{w=0}^{W-1} \|G_{\mathbf{C}^{t+w}}(\mathbf{B}) - \mathbf{x} + \mathbf{x} - \frac{1}{W} \sum_{j=0}^{W-1} G_{\mathbf{C}^{t+j}}(\mathbf{B})\|_2^2 \quad (\text{A21})$$

$$\leq \left( \frac{2}{W} \sum_{w=0}^{W-1} \|G_{\mathbf{C}^{t+w}}(\mathbf{B}) - \mathbf{x}\|_2^2 \right) + 2\|\mathbf{x} - \frac{1}{W} \sum_{j=0}^{W-1} G_{\mathbf{C}^{t+j}}(\mathbf{B})\|_2^2 \quad (\text{A22})$$

$$\leq \frac{2}{W} \sum_{w=0}^{W-1} \|G_{\mathbf{C}^{t+w}}(\mathbf{B}) - \mathbf{x}\|_2^2 + \frac{2}{W} \sum_{j=0}^{W-1} \|G_{\mathbf{C}^{t+j}}(\mathbf{B}) - \mathbf{x}\|_2^2 \quad (\mathbf{z} \mapsto \|\mathbf{z} - \mathbf{x}\|_2^2 \text{ convex and Jensen's inequality}) \quad (\text{A23})$$

$$= \frac{4}{W} \sum_{w=0}^{W-1} \|G_{\mathbf{C}^{t+w}}(\mathbf{B}) - \mathbf{x}\|_2^2. \quad (\text{A24})$$

In view of [Theorem A.1](#),

$$\|G_{\mathbf{C}^{t+w}}(\mathbf{B}) - \mathbf{x}\|_2^2 \leq 3 \left(1 - \eta\sigma_p^2\right)^{2t+2w} \|\mathbf{x}\|_2^2 + 3 \sum_{i=1}^n \left( \left(1 - \eta\sigma_i^2\right)^{t+w} - 1 \right)^2 (\mathbf{w}_i^\top \mathbf{n})^2 + 3\varepsilon^2 \|\mathbf{y}\|_2^2. \quad (\text{A25})$$

Thus,

$$\begin{aligned} & \sum_{w=0}^{W-1} \|G_{\mathbf{C}^{t+w}}(\mathbf{B}) - \mathbf{x}\|_2^2 \\ & \leq 3\|\mathbf{x}\|_2^2 \sum_{w=0}^{W-1} \left(1 - \eta\sigma_p^2\right)^{2t+2w} + 3 \sum_{w=0}^{W-1} \sum_{i=1}^n \left( \left(1 - \eta\sigma_i^2\right)^{t+w} - 1 \right)^2 (\mathbf{w}_i^\top \mathbf{n})^2 + 3W\varepsilon^2 \|\mathbf{y}\|_2^2 \end{aligned} \quad (\text{A26})$$

$$\leq 3\|\mathbf{x}\|_2^2 \frac{(1 - \eta\sigma_p^2)^{2t} (1 - (1 - \eta\sigma_p^2)^{2W})}{1 - (1 - \eta\sigma_p^2)^2} + 3W \sum_{i=1}^n \left( \left(1 - \eta\sigma_i^2\right)^{t+W-1} - 1 \right)^2 (\mathbf{w}_i^\top \mathbf{n})^2 + 3W\varepsilon^2 \|\mathbf{y}\|_2^2 \quad (\text{A27})$$

$$\leq 3\|\mathbf{x}\|_2^2 \frac{(1 - \eta\sigma_p^2)^{2t}}{1 - (1 - \eta\sigma_p^2)^2} + 3W \sum_{i=1}^n \left( \left(1 - \eta\sigma_i^2\right)^{t+W-1} - 1 \right)^2 (\mathbf{w}_i^\top \mathbf{n})^2 + 3W\varepsilon^2 \|\mathbf{y}\|_2^2, \quad (\text{A28})$$

completing the proof.  $\square$

## References

Abdelhamed, A., Afifi, M., Timofte, R., Brown, M.S., Cao, Y., Zhang, Z., ... Kumar, V. (2020). Ntire 2020 challenge on real image denoising: Dataset, methods and results. *arXiv:2005.04117*.

- Asim, M., Shamsad, F., & Ahmed, A. (2019). Blind image deconvolution using deep generative priors. *arXiv:1802.04073*.
- Baguer, D.O., Leuschner, J., & Schmidt, M. (2020, Sep). Computed tomography reconstruction using deep image prior and learned reconstruction methods. *Inverse Problems*, 36(9), 094004. Retrieved from <http://dx.doi.org/10.1088/1361-6420/aba415> 10.1088/1361-6420/aba415
- Bahrami, K., & Kot, A.C. (2014, jun). A fast approach for no-reference image sharpness assessment based on maximum local variation. *IEEE Signal Processing Letters*, 21(6), 751–755. 10.1109/lsp.2014.2314487
- Cascarano, P., Sebastiani, A., Comes, M.C., Franchini, G., & Porta, F. (2021). Combining weighted total variation and deep image prior for natural and medical image restoration via admm. *arXiv:2009.11380*.
- Cheng, Z., Gadelha, M., Maji, S., & Sheldon, D. (2019a). A bayesian perspective on the deep image prior. *arXiv:1904.07457*.
- Cheng, Z., Gadelha, M., Maji, S., & Sheldon, D. (2019b, jun). A bayesian perspective on the deep image prior. In *Cvpr*. IEEE. 10.1109/cvpr.2019.00559
- Chizat, L., Oyallon, E., & Bach, F. (2018, December). On lazy training in differentiable programming. *Advances in Neural Information Processing Systems (NeurIPS), Dec 2019, Vancouver, Canada*.
- Crete, F., Dolmiere, T., Ladret, P., & Nicolas, M. (2007, feb). The blur effect: perception and estimation with a new no-reference perceptual blur metric. In B.E. Rogowitz, T.N. Pappas, & S.J. Daly (Eds.), *SPIE proceedings*. SPIE. 10.1117/12.702790
- Dabov, K., Foi, A., Katkovnik, V., & Egiazarian, K. (2007, aug). Image denoising by sparse 3-d transform-domain collaborative filtering. *IEEE Transactions on Image Processing*, 16(8), 2080–2095. 10.1109/tip.2007.901238
- Darestani, M.Z., & Heckel, R. (2021). Accelerated mri with un-trained neural networks. *IEEE Transactions on Computational Imaging*, 7, 724–733.
- Ding, L., Jiang, L., Chen, Y., Qu, Q., & Zhu, Z. (2021, September). Rank overspecified robust matrix recovery: Subgradient method and exact recovery. *arXiv:2109.11154*.
- Gandelsman, Y., Shocher, A., & Irani, M. (2019, June). "double-dip": Unsupervised image decomposition via coupled deep-image-priors. In *Cvpr*.
- Gong, K., Catana, C., Qi, J., & Li, Q. (2021). Direct reconstruction of linear parametric images from dynamic pet using nonlocal deep image prior. *arXiv:2106.10359*.
- Hand, P., Leong, O., & Voroninski, V. (2018). Phase retrieval under a generative prior. *arXiv:1807.04261*.
- Hashimoto, F., & Ote, K. (2021). Direct pet image reconstruction incorporating deep image prior and a forward projection model. *arXiv:2109.00768*.
- Heckel, R., & Hand, P. (2018). Deep decoder: Concise image representations from untrained non-convolutional networks. *arXiv preprint arXiv:1810.03982*.

- Heckel, R., & Soltanolkotabi, M. (2020a, 13–18 Jul). Compressive sensing with un-trained neural networks: Gradient descent finds a smooth approximation. In H.D. III & A. Singh (Eds.), *Proceedings of the 37th international conference on machine learning* (Vol. 119, pp. 4149–4158). PMLR. Retrieved from <https://proceedings.mlr.press/v119/heckel20a.html>
- Heckel, R., & Soltanolkotabi, M. (2020b). Denoising and regularization via exploiting the structural bias of convolutional generators. In *Iclr*.
- Hendrycks, D., & Dietterich, T. (2019). Benchmarking neural network robustness to common corruptions and perturbations. *Proceedings of the International Conference on Learning Representations*.
- Jacot, A., Gabriel, F., & Hongler, C. (2018, June). Neural tangent kernel: Convergence and generalization in neural networks. In *Advances in neural information processing systems (pp. 8571-8580) 2018*.
- Janai, J., Güney, F., Behl, A., & Geiger, A. (2020). Computer vision for autonomous vehicles: Problems, datasets and state of the art. *Foundations and Trends® in Computer Graphics and Vision*, 12(1–3), 1–308. 10.1561/06000000079
- Jo, Y., Chun, S.Y., & Choi, J. (2021). Rethinking deep image prior for denoising. *arXiv:2108.12841*.
- Krishnan, D., Tay, T., & Fergus, R. (2011). Blind deconvolution using a normalized sparsity measure. In *Cvpr* (pp. 233–240).
- Levin, A., Weiss, Y., Durand, F., & Freeman, W.T. (2011). Understanding blind deconvolution algorithms. *IEEE transactions on pattern analysis and machine intelligence*, 33(12), 2354–2367.
- Li, T., Zhuang, Z., Liang, H., Peng, L., Wang, H., & Sun, J. (2021). Self-validation: Early stopping for single-instance deep generative priors. In *The british machine vision conference (bmvc)*.
- Liu, C., Zhu, L., & Belkin, M. (2020, October). On the linearity of large non-linear models: when and why the tangent kernel is constant. *arXiv:2010.01092*.
- Liu, J., Sun, Y., Xu, X., & Kamilov, U.S. (2018). Image restoration using total variation regularized deep image prior. *arXiv:1810.12864*.
- Ma, X., Hill, P., & Achim, A. (2021, October). Unsupervised image fusion using deep image priors. *arXiv:2110.09490*.
- Martin, D., Fowlkes, C., Tal, D., & Malik, J. (2001). A database of human segmented natural images and its application to evaluating segmentation algorithms and measuring ecological statistics. In *Proceedings eighth IEEE international conference on computer vision. ICCV 2001*. IEEE Comput. Soc. 10.1109/iccv.2001.937655
- Mataev, G., Milanfar, P., & Elad, M. (2019). Deepred: Deep image prior powered by red. In *Proceedings of the IEEE/CVF international conference on computer vision workshops* (pp. 0–0).
- Metzler, C.A., Mousavi, A., Heckel, R., & Baraniuk, R.G. (2018, May). Unsupervised learning with stein’s unbiased risk estimator. *arXiv:1805.10531*.
- Mittal, A., Moorthy, A.K., & Bovik, A.C. (2012). No-reference image quality assessment in the spatial domain. *IEEE Transactions on image processing*, 21(12), 4695–4708.
- Mittal, A., Soundararajan, R., & Bovik, A.C. (2012). Making a “completely blind” image quality analyzer.

*IEEE Signal processing letters*, 20(3), 209–212.

- Ongie, G., Jalal, A., Metzler, C.A., Baraniuk, R.G., Dimakis, A.G., & Willett, R. (2020, may). Deep learning techniques for inverse problems in imaging. *IEEE Journal on Selected Areas in Information Theory*, 1(1), 39–56. 10.1109/jsait.2020.2991563
- Qayyum, A., Ilahi, I., Shamshad, F., Boussaid, F., Bennamoun, M., & Qadir, J. (2021, mar). Untrained neural network priors for inverse imaging problems: A survey. *TechRxiv*. 10.36227/techrxiv.14208215.v1
- Ren, D., Zhang, K., Wang, Q., Hu, Q., & Zuo, W. (2020, June). Neural blind deconvolution using deep priors. In *Cvpr*.
- Shi, Z., Mettes, P., Maji, S., & Snoek, C.G.M. (2021). On measuring and controlling the spectral bias of the deep image prior. *arXiv:2107.01125*.
- Sitzmann, V., Martel, J., Bergman, A., Lindell, D., & Wetzstein, G. (2020). Implicit neural representations with periodic activation functions. *Advances in Neural Information Processing Systems*, 33.
- Sun, Z. (2021). Solving inverse problems with hybrid deep image priors: the challenge of preventing overfitting. *arXiv:2011.01748*.
- Szeliski, R. (2021). *Computer vision* (2nd ed.). Springer London. 10.1007/978-1-84882-935-0
- Talebi, H., & Milanfar, P. (2018). Nima: Neural image assessment. *IEEE Transactions on Image Processing*, 27(8), 3998–4011.
- Tayal, K., Manekar, R., Zhuang, Z., Yang, D., Kumar, V., Hofmann, F., & Sun, J. (2021). Phase retrieval using single-instance deep generative prior. In *OSA optical sensors and sensing congress 2021 (AIS, FTS, HISE, SENSORS, ES)*. OSA. 10.1364/ais.2021.jw2a.37
- Tran, P., Tran, A.T., Phung, Q., & Hoai, M. (2021, jun). Explore image deblurring via encoded blur kernel space. In *Cvpr*. IEEE. 10.1109/cvpr46437.2021.01178
- Ulyanov, D., Vedaldi, A., & Lempitsky, V. (2018). Deep image prior. In *Cvpr* (pp. 9446–9454).
- Vaškevičius, T., Kanade, V., & Rebeschini, P. (2019). *Implicit regularization for optimal sparse recovery*. arXiv. 10.48550/ARXIV.1909.05122
- Veen, D.V., Jalal, A., Soltanolkotabi, M., Price, E., Vishwanath, S., & Dimakis, A.G. (2020). Compressed sensing with deep image prior and learned regularization. *arXiv:1806.06438*.
- Wang, Z., Wang, Z., Li, Q., & Bilen, H. (2019). Image deconvolution with deep image and kernel priors. *arXiv:1910.08386*. IEEE International Conference on Computer Vision Workshops.
- Williams, F., Schneider, T., Silva, C., Zorin, D., Bruna, J., & Panozzo, D. (2019). Deep geometric prior for surface reconstruction. *arXiv:1811.10943*.
- Yoo, J., Jin, K.H., Gupta, H., Yerly, J., Stuber, M., & Unser, M. (2021). Time-dependent deep image prior for dynamic mri. *arXiv:1910.01684*.
- You, C., Zhu, Z., Qu, Q., & Ma, Y. (2020). Robust recovery via implicit bias of discrepant learning rates for double over-parameterization. *arXiv:2006.08857*.



- Zbontar, J., Knoll, F., Sriram, A., Murrell, T., Huang, Z., Muckley, M.J., . . . Lui, Y.W. (2018, November). fastmri: An open dataset and benchmarks for accelerated mri. *arXiv:1811.08839*.
- Zhuang, Z., Li, T., Wang, H., & Sun, J. (2022). *Blind image deblurring with unknown kernel size and substantial noise*. (Forthcoming)